Potential vorticity structure of embedded convection in a warm conveyor belt and its relevance for the large-scale dynamics

Annika Oertel[1], Maxi Boettcher[1], Hanna Joos[1], Michael Sprenger[1], and Heini Wernli[1]

[1]IAC, ETH Zürich, Zürich, Switzerland

Correspondence: Annika Oertel (annika.oertel@env.ethz.ch)

Abstract. Warm conveyor belts (WCBs) are important airstreams in extratropical cyclones. They can influence the large-scale flow evolution due to the modification of the potential vorticity (PV) distribution during their cross-isentropic ascent. Although WCBs are typically described as slantwise ascending and stratiform cloud producing airstreams, recent studies identified convective activity embedded within the large-scale WCB cloud band. Yet, the impacts of this WCB-embedded convection have not been investigated in detail. In this study, we systematically analyse the influence of embedded convection in an eastern North Atlantic WCB on the cloud and precipitation structure, on the PV distribution, and on the larger-scale flow. For this, we apply online trajectories in a high-resolution convection-permitting simulation and perform a composite analysis to compare quasi-vertically ascending convective WCB trajectories with typical slantwise ascending WCB trajectories. We find that the convective WCB ascent leads to stronger surface precipitation including the formation of graupel, which is absent for the slantwise WCB category, indicating the key role of WCB-embedded convection for precipitation extremes. Compared to the slantwise WCB trajectories, the initial equivalent potential temperature of the convective WCB trajectories is higher and they originate from a region of larger potential instability, which gives rise to more intense cloud diabatic processes and stronger cross-isentropic ascent. Moreover, the signature of embedded convection is distinctly imprinted in the PV structure. The diabatically generated low-level positive PV anomalies, associated with a cyclonic circulation anomaly, are substantially stronger for the convective WCB trajectories. While the slantwise WCB trajectories form a wide-spread negative PV anomaly (but still with weakly positive PV values) in the upper troposphere, in agreement with previous studies, the convective WCB trajectories, in contrast, form mesoscale horizontal PV dipoles at upper levels, with one pole reaching negative PV. On the larger-scale, these individual mesoscale PV anomalies can aggregate to elongated PV dipole bands extending from the convective updraft region, which are associated with coherent larger-scale circulation anomalies. An illustrative example of such a convectively generated PV dipole band shows that within around 10 hours the negative PV pole is advected closer to the upper-level waveguide, where it strengthens the isentropic PV gradient and contributes to the formation of a jet streak. This suggests that the mesoscale PV anomalies produced by embedded convection upstream organise and persist for several hours, and therefore can influence the synoptic-scale circulation. They thus can be dynamically relevant. Finally, our results imply that a distinction between slantwise and convective WCB trajectories is meaningful because the convective WCB trajectories are characterized by distinct properties, such as the formation of graupel and of an upper-level PV dipole, which are absent for slantwise WCB trajectories.

1 Introduction

Moist diabatic processes in extratropical cyclones are known to play an important role for their evolution and are frequently associated with rapid cyclogenesis (e.g., Anthes et al., 1983; Kuo et al., 1991; Stoelinga, 1996; Wernli and Davies, 1997) and increased forecast error growth (e.g., Davies and Didone, 2013; Selz and Craig, 2015). Diabatic processes are partic-

30   ularly important in warm conveyor belts (WCBs), which are coherent, typically poleward ascending airstreams associated with extratropical cyclones (Harrold, 1973; Browning, 1986, 1999; Wernli and Davies, 1997). During their typically slantwise cross-isentropic ascent from the boundary layer ahead of the cold front to the upper troposphere, they form large-scale mostly stratiform cloud bands and play a key role for the distribution of surface precipitation (e.g., Browning, 1986; Eckhardt et al., 2004; Madonna et al., 2014; Pfahl et al., 2014; Flaounas et al., 2018). Furthermore, the strong cloud diabatic processes during

35   WCB ascent modify the potential vorticity (PV) distribution in the lower and upper troposphere and thereby potentially affect the large-scale flow evolution (e.g., Wernli and Davies, 1997; Wernli, 1997; Madonna et al., 2014; Joos and Forbes, 2016).

PV is materially conserved along the flow only in the absence of friction and diabatic processes (Hoskins et al., 1985). Neglecting frictional processes, the Lagrangian rate of change $\frac{D}{Dt}PV$ can be expressed as

$$\frac{D}{Dt}PV = \frac{1}{\rho}\boldsymbol{\omega} \cdot \nabla\dot{\theta}, \tag{1}$$

40   where PV is defined as

$$PV = \frac{1}{\rho}\boldsymbol{\omega} \cdot \nabla\theta \tag{2}$$

and ρ is density, θ is potential temperature and $\boldsymbol{\omega}$ is 3D absolute vorticity ($\boldsymbol{\omega} = \nabla \times \mathbf{u} + 2\boldsymbol{\Omega} = \xi\mathbf{i} + \eta\mathbf{j} + (f + \zeta)\mathbf{k}$).

For large-scale and predominantly slantwise WCB ascent it is frequently assumed that the first-order effect of latent heating on PV is dominated by the vertical gradient of diabatic heating (e.g., Wernli and Davies, 1997; Joos and Wernli, 2012; Madonna

45   et al., 2014) resulting in PV generation below and PV destruction above the diabatic heating maximum according to Eq. 3:

$$\frac{D}{Dt}PV \approx \frac{1}{\rho}(f + \zeta) \cdot \frac{\partial\dot{\theta}}{\partial z}. \tag{3}$$

These diabatically produced low-level positive and upper-level negative PV anomalies can lead to cyclone intensification (Rossa et al., 2000; Binder et al., 2016) and modify the upper-level flow evolution (Pomroy and Thorpe, 2000; Grams et al., 2011; Schäfler and Harnisch, 2015; Joos and Forbes, 2016; Martínez-Alvarado et al., 2016).

50   PV is frequently considered for synoptic-scale dynamics (e.g., Hoskins et al., 1985; Stoelinga, 1996), but is also suited for the analysis of mesoscale convective systems (e.g., Pomroy and Thorpe, 2000; Martínez-Alvarado et al., 2016; Shutts, 2017; Clarke et al., 2019) and has already been applied at the scale of convective storms (Chagnon and Gray, 2009; Weijenborg et al., 2015, 2017). While for PV modification in synoptic-scale systems the horizontal gradients of diabatic heating are frequently neglected (as in Eq. 3), this assumption breaks down in the case of intense local diabatic heating such as embedded mesoscale

55 convective updrafts on the scale of a few kilometers. There the horizontal gradients of $\dot{\theta}$ become relevant and Eq. 3 generalizes
to the full form, Eq. 2, written here as

$$\frac{D}{Dt}PV = \frac{1}{\rho}\left[(f+\zeta)\frac{\partial\dot{\theta}}{\partial z} + \boldsymbol{\omega}_h \cdot \nabla_h\dot{\theta}\right].\tag{4}$$

In contrast to the WCB, where the vertical gradient dominates, the horizontal diabatic heating gradient plays a major role for
the PV modification in isolated (mesoscale) convective updrafts (e.g., Chagnon and Gray, 2009; Weijenborg et al., 2015, 2017).
60 The localized diabatic heating in convective updrafts in a vertically sheared environment generates upper-level horizontal PV
dipoles centered around the convective updraft and aligned with the horizontal vorticity vector $\boldsymbol{\omega}_\mathrm{h}$ (Eq. 4). Thereby, the positive
PV pole occurs to the right of the direction of the thermal wind vector $\mathbf{v_T}$ (since there, $\nabla_h\dot{\theta}$ is parallel to $\boldsymbol{\omega}_\mathrm{h}$) and the negative
pole occurs to the left of $\mathbf{v_T}$ (where $\nabla_h\dot{\theta}$ and $\boldsymbol{\omega}_\mathrm{h}$ are antiparallel), as illustrated in Fig. 1. This tilting of the PV dipole
from the vertical, as typically observed for large-scale WCB ascent, into the horizontal is a robust response of convective
65 updrafts in the presence of vertical wind shear (Chagnon and Gray, 2009; Weijenborg et al., 2015, 2017; Hitchman and Rowe,
2017). Such convectively generated PV dipoles were previously identified in idealized simulations of isolated cumulus-scale
convection (Chagnon and Gray, 2009), in case studies of mesoscale convective systems (Davis and Weisman, 1994; Chagnon
and Gray, 2009; Hitchman and Rowe, 2017; Clarke et al., 2019), and in mid-latitude convective updrafts with varying large-
scale flow conditions (Weijenborg et al., 2015, 2017). The amplitudes of the horizontal PV dipoles can strongly exceed the
70 typical amplitude of synoptic-scale PV. In strong convective updrafts horizontal PV dipoles of $\pm 10\,\mathrm{PVU}$ can be generated
(Chagnon and Gray, 2009; Weijenborg et al., 2015, 2017), resulting in regions of absolute negative PV, which are dynamically
unstable. These regions can be hydrostatically, inertially or symmetrically unstable (Schultz and Schumacher, 1999) and can
form mesoscale circulations associated, e.g., with frontal rainbands (Bennetts and Hoskins, 1979; Schultz and Schumacher,
1999; Siedersleben and Gohm, 2016), sting jets (Clark et al., 2005; Volonté et al., 2018), enhanced stratosphere-troposphere
75 exchange (Rowe and Hitchman, 2015), and local jet accelerations and northward displacements (Rowe and Hitchman, 2016).
The adjustment timescales for the release of these instabilities ranges from minutes for hydrostatic instability to several hours
for inertial instability [scales with $[-f(f+\zeta)]^{-1/2}$; Schultz and Schumacher (1999); Thompson et al. (2018)]. Thus, while
hydrostatic instability is rapidly released and near-neutral conditions are established, inertial instability can prevail for several
hours and therefore synoptic-scale regions of inertial instability can be observed, for instance at the anticyclonic shear side of
80 midlatitude ridges (Thompson et al., 2018).

Although WCBs are typically described as gradually ascending and mainly stratiform cloud producing airstreams (e.g.,
Browning, 1986; Madonna et al., 2014), already in 1993 the concept of rapid convective motion embedded in the frontal
cloud band of the WCB was proposed (Neiman et al., 1993). Recently, studies suggested that the WCB is, at least in some
cases, not a homogeneously ascending airstream: in contrast, the detailed ascent behaviour of the individual WCB trajectories
85 associated with one extratropical cyclone can vary substantially (e.g., Martínez-Alvarado et al., 2014; Rasp et al., 2016; Oertel
et al., 2019) and convective activity can be frequently embedded in the large-scale baroclinic region of the WCB. This has
been identified, e.g., with remote-sensing data (Binder, 2016; Crespo and Posselt, 2016; Flaounas et al., 2016, 2018), with

online trajectories in convection-resolving simulations (Rasp et al., 2016; Oertel et al., 2019) and in coarser simulations with parameterized convection (Agustì-Panareda et al., 2005; Martínez-Alvarado and Plant, 2014). WCBs and convective systems
90 can both lead to forecast errors due to their associated strong diabatic processes (e.g., Martínez-Alvarado et al., 2016; Clarke et al., 2019). Ocassionally, this might even lead to forecast busts (Rodwell et al., 2013), especially in coarser-scale simulations where the PV anomaly amplitude is underestimated due to the parameterization of convection (Done et al., 2006; Chagnon and Gray, 2009; Clarke et al., 2019).

Although previous studies analysed the PV modification by individual convective updrafts, the PV modification by ag-
95 gregated convection embedded in the WCB ascent region, which is already subject to strong diabatic PV modification from large-scale WCB ascent, has not yet been investigated. Moreover, the persistence and dynamical relevance of the convectively generated PV dipoles has not yet been analysed. Weijenborg et al. (2017) hypothesized that the convectively formed large-amplitude PV anomalies could be longer-lived than the relatively short-lived convective updrafts and suggested that a more detailed investigation of these PV anomalies might shed light on the dynamical relevance of convection. Related to this is the
100 question whether the convectively generated PV dipoles aggregate to larger-scale PV anomalies and, if yes, whether they feed back on the synoptic-scale flow (Chagnon and Gray, 2009).

In this study we investigate convection embedded in WCBs and systematically analyse the PV modification of this convective activity. Furthermore, we go beyond the identification of convectively produced PV anomalies and evaluate the effect of these mesoscale PV anomalies on the larger-scale flow. Therefore, we compute online trajectories in a high-resolution convection-
105 permitting simulation to compare convective and slantwise WCB trajectories and their impact on the cloud and precipitation structure, as well as the mesoscale and larger-scale dynamics. Specifically, we adress the following questions:

1. Where do convective and slantwise WCB trajectories originate from and how does their ascent differ (section 3.2)?

2. What is the impact of convective WCB ascent on the cloud and precipitation structure (section 3.3)?

3. How does convective (vs. slantwise) WCB ascent modify the PV distribution along the ascent and in its environment
110   (section 3.4)?

4. What is the influence of convectively modified PV on the local wind speed and circulation in the upper troposphere (section 3.5)?

5. How does convection embedded in WCBs and its associated PV anomalies influence the larger-scale dynamics (section 5)?

115 This study is structured in the following way: In section 2, we explain the methodology and shortly introduce the WCB case study. Thereafter, we systematically consider the mesoscale effects of convection embedded in WCBs (questions 1-4) in a composite analysis (section 3), before discussing an illustrative example of the characteristics and impact of convective ascent embedded in the WCB (section 4). To adress the question of the dynamical relevance of WCB-embedded convection (question 5), we consider the convectively generated PV anomalies on a larger scale and evaluate their influence on the large-
120 scale flow (section 5). Finally, we provide a discussion and outlook (section 6) and conclusions (section 7).

2 Data and approach

2.1 COSMO setup and trajectories

The setup of the COSMO simulation and the online trajectories used to address the questions outlined in section 1 is the same as in Oertel et al. (2019). The WCB case study was simulated with the nonhydrostatic model COSMO (Baldauf et al., 2011;
125 Doms and Baldauf, 2015) at $0.02°$ (2.2 km) horizontal resolution with 60 vertical levels. The simulation was initialised at 00 UTC 22 Sep 2016 in the early phase of the cyclogenesis of "Vladiana" (see section 2.2) and run for 112 hours (see Oertel et al., 2019). Initial and lateral boundary conditions are taken from the ECMWF analyses with a horizontal resolution of $0.1°$ every 6 hours. The domain is centered in the eastern North Atlantic and extends from about $50°$W to $20°$E and $30°$N to $70°$N. We applied the standard COSMO setup of the Swiss National Weather Service, which employs a one-moment six-category
130 cloud microphysics scheme including prognostic water vapour (q_v), liquid (LWC) and ice cloud water content (IWC), rain (LWC), snow (SWC) and graupel (GWC). The graupel category is important for the explicit simulation of deep convection (Baldauf et al., 2011). Deep convection is resolved at 2.2 km (e.g., Ban et al., 2014) while for shallow convection the reduced Tiedtke scheme was applied (Tiedtke, 1989; Baldauf et al., 2011). 3D COSMO fields were output every 15 minutes, which allows capturing the large temporal and spatial variability of embedded convection.

135 To identify phases of embedded convective ascent in the WCB, 10 000 online trajectories were started from a predefined starting region at 7 vertical levels (250, 500, 750, 1000, 1500, 2000 and 2500 m a.s.l.) every 2 h during the simulation (Miltenberger et al., 2013, 2014). The online trajectory positions are calculated from the resolved 3D wind field at every model time step, i.e. every 20 s, and thus, explicitly capture rapid convective ascent (Miltenberger et al., 2013; Rasp et al., 2016; Oertel et al., 2019). WCB trajectories were calculated as trajectories with an ascent rate of at least 600 hPa in 48 h (Madonna et al.,
140 2014).

2.2 Overview of WCB case study

The investigated WCB was associated with the North Atlantic extratropical cyclone "Vladiana" (IOP 3 of NAWDEX, Schäfler et al., 2018) from 22-25 Sep 2016. The cyclone with a maximum intensity of 975 hPa is located below an upper-level trough and travels eastward and northward across the North Atlantic toward Iceland, where it becomes stationary. The cyclone's WCB
145 ascends in the warm sector predominantly in a narrow band ahead of the cold front and develops a weak cyclonic and a stronger anticyclonic branch (cf. Wernli, 1997; Martínez-Alvarado et al., 2014), which turns into the downstream upper-level ridge and contributes to its amplification. For a more detailed analysis of the cyclone evolution and its WCB ascent see Oertel et al. (2019).

The WCB trajectories in the baroclinic zone ahead of the cyclone's cold front vary considerably in their ascent rates and
150 also include phases of embedded convection. These phases are characterized by a rapid ascent of more than 400-600 hPa in 2 h, and they are embedded in a larger region of slower, more gradual WCB ascent (Oertel et al., 2019). The region of embedded convective activity is characterized by a very heterogeneous PV field of diabatically-produced small-scale but high-amplitude PV anomalies of ± 10 PVU in the upper troposphere (cf. Fig. 8d; Oertel et al., 2019, Appendix), suggesting that embedded

convection in WCBs can strongly modify the PV distribution. There is, however, no clear separation between convective and

155   slantwise ascent in the WCB of cyclone "Vladiana" (Oertel et al., 2019). Instead, it is rather a continuum of ascent rates ranging from very rapid convective ascent of more than 600 hPa in 2 h to a slower gradual ascent of approximately 50 hPa in 2 h. Nevertheless, we can meaningfully classify the WCB trajectories into two categories based on their ascent rate to compare convective versus slantwise WCB ascent (see section 2.3).

2.3   WCB trajectory categorisation and WCB ascent region

160   To compare the rapid convective WCB ascent to the "typical" more slowly and slantwise WCB ascent, we selected two categories of coherently ascending WCB trajectories from all WCB trajectories associated with the cyclone: (i) convectively ascending WCB trajectories that perform a rapid quasi-vertical ascent through the whole tropospheric column and (ii) slantwise WCB trajectories that ascend more slowly and gradually from the boundary layer into the upper troposphere. The selection criteria are based on the fastest 400-hPa and 600-hPa ascent phases along the WCB trajectories: a WCB trajectory is consid-

165   ered as convective if its fastest 400-hPa and 600-hPa ascent times are shorter than 1 h and 3 h, respectively. These ascent rates correspond to the 10% fastest ascent rates of all trajectories of the considered WCB. Likewise, a WCB trajectory is assigned to the slantwise WCB category if the 400-hPa and 600-hPa ascent times are between 1.5 h to 3.5 h and 6.5 h to 22 h, respectively. These ascent times correspond to the average ascent rates of all WCB trajectories (25th to 75th percentiles). These selection criteria result in approximately 2000 convective WCB trajectories, and approximately 7000 more slowly ascending slantwise

170   WCB trajectories. Figure 2a shows the temporal evolution of the WCB trajectory positions at the start of their ascent relative to the approaching cold front for selected time steps and illustrates the main WCB ascent region ahead of the cold front and the upper-level trough. The convective WCB trajectories perform a rapid and deep ascent through the whole tropospheric column mostly south of 50°N (Fig. 2a, black outlined circles), and the slantwise WCB trajectories with comparatively slow and gradual WCB ascent are located ahead of, and travel northward with, the cold front during their ascent (Fig. 2a, grey outlined

175   triangles). During the 3 days of major WCB ascent from 22 Sep to 24 Sep 2016, the region of ascent shifts about 20° eastward with the evolving cyclone and its cold front (see coloured symbols in Fig. 2a). Despite the differing ascent behaviour of the WCB categories, the convective WCB ascent is directly embedded in the region of large-scale ascent, i.e., in close proximity to the more slowly ascending WCB trajectories. This indicates that although their ascent rates differ, both WCB categories are not spatially separated (Fig. 2a).

180 ## 3   Characteristics of convective and slantwise WCB ascent

3.1   Composite computation

The similarities and differences of the characteristics of convective and slantwise WCB trajectories are systematically compared in a composite analysis. For computing composites for both WCB categories, the selected WCB trajectories were centered

relative to the time of the start of the fastest 400-hPa ascent phase. Composites were computed based on the trajectory position
185 every 15-minutes, which corresponds to the temporal resolution of the COSMO output.

Three types of composites were produced for both WCB categories: (i) composites of vertical profiles along the trajectories,
i.e. time-height sections along the flow, (ii) horizontal and (iii) vertical cross-sections centered at the trajectories' geographical
position. While the along-flow composites provide a Lagrangian perspective on the local dynamical impact of the WCB trajec-
tories, the horizontal and vertical cross-sections allow analysing their effect on the surroundings. Because the trajectories are
190 located in a region with coherent background flow ahead of the upper-level trough, the fields were not rotated for the composite
computation. This enables a direct interpretation of the atmospheric conditions and perturbations in geographic coordinates.

The number of selected convective and slantwise WCB trajectories is not homogeneous in time; instead pulses of convective
and slantwise WCB ascent occur (Fig. 2b and cf. Oertel et al., 2019). In particular, two pulses of increased convective activity
occur at around 00 UTC 23 Sep and 00 UTC 24 Sep. Hence, the composite analyses are dominated by these times when large
195 numbers of WCB trajectories are selected for each category.

In the following, we first compare the ascent behavior and environment of convective and slantwise WCB trajectories (sec-
tion 3.2) and subsequently describe the precipitation and cloud structure associated with both WCB categories (section 3.3).
Next, the PV structure associated with convective and slantwise WCB ascent is shown (section 3.4) and related to the larger-
scale flow anomalies (section 3.5).

200 **3.2 Environment for convective and slantwise WCB ascent**

The rapidly ascending convective WCB trajectories originate from a warmer and moister region ($\overline{T} = 287\,\text{K}, \overline{q_v} = 11.5\,\text{g kg}^{-1}$)
compared to the more slowly ascending slantwise WCB trajectories ($\overline{T} = 285\text{K}, \overline{q_v} = 10\,\text{g kg}^{-1}$), and are thus characterized by
substantially higher initial θ_e (Figs. 3a and 4a) than the slantwise WCB trajectories (Figs. 3b and 4b). At the start of the ascent,
$\overline{\theta_\text{e}}$ amounts to 330 K for the convective WCB trajectories and to 324 K for the slantwise WCB trajectories (Fig. 4a,b). Although
205 the convective ascent is embedded within the region of slantwise ascent ahead of the cold front (Fig. 2), where θ_e-contours
nearly become vertical (Fig. 3c,d), the convective WCB trajectories ascend from a mesoscale, meridionally elongated region
characterized by warmer and more humid conditions ahead of a strong localised θ_e-gradient (Fig. 3a). This narrow tongue of
very high θ_e air with q_v exceeding $11\,\text{g kg}^{-1}$ extends laterally from ahead of the cold front only approximately 50 km into the
warm sector and forms a strong horizontal θ_e gradient (Fig. 3a). Moreover, the WCB ascent region ahead of the cold frontal
210 zone coincides with low-level convergence of the horizontal wind (Fig. 3c,d), which is particularly strong for the convective
WCB trajectories. The mesoscale frontal θ_e structures ahead of the cold front arise from large θ_e variability in the warm sector.
The higher θ_e of the convective WCB trajectories subsequently leads to more intense cloud diabatic processes and a faster and
stronger cross-isentropic ascent (Fig. 4a,b).

The convective WCB trajectories ascend rapidly from the boundary layer to the upper troposphere to on average 10 km
215 height in about 1-2 h (Fig. 4a) from a region of strong potential instability characterized by vertical θ_e gradients of $-4\,\text{K km}^{-1}$
prior to the start of the convective ascent (Fig. 4c), and continue to moderately ascend almost isentropically along the upper-
level ridge after arriving in the upper troposphere (Fig. 4a). The convective WCB ascent is likely triggered through lifting of the

potentially unstable layer in the frontal ageostrophic circulation (cf. quasi-geostrophic omega ahead of cold front, Oertel et al., 2019). During an initial adiabatic ascent the low-level potentially unstable layer in the WCB inflow region remains potentially

220   unstable until saturation is reached at the lifting condensation level. There, the potential instability can be released leading to the observed rapid convective updrafts (Schultz and Schumacher, 1999; Sherwood, 2000; Schultz et al., 2000).

In contrast, the slower slantwise WCB trajectories start their ascent from the boundary layer in a region characterized by weaker potential instability and lower relative humidity (Fig. 4d) and ascend on top of the (cold) frontal region characterized by comparatively large potential stability (Fig. 4b,d). After an initially swift ascent (due to the centering relative to the fastest

225   400-hPa ascent), the ascent rate decreases and the trajectories perform a gradual slantwise ascent until they reach their final outflow level at on average 9 km height after approximately 18 h. Hence, the final WCB outflow height of the slantwise WCB trajectories is on average lower compared to the convective WCB trajectories that reach on average approximately 10 km height.

3.3   Precipitation and cloud structure

230   During their rapid ascent the convective WCB trajectories locally produce intense surface precipitation (Fig. 5a,c, blue lines). The precipitation maximum coincides with the strongest ascent phase in the mid-troposphere, where also a local maximum of graupel production occurs (Fig. 5c, magenta contours). The convective cloud is characterized by a large hydrometeor content of up to $1 \, \mathrm{g \, kg^{-1}}$ (Fig. 5c) and the vertically integrated rain, snow and graupel water path in close proximity to the updraft can reach up to $6 \, \mathrm{kg \, m^{-2}}$ (Fig. 5a), forming a locally dense and vertically extended cloud (Fig. 5c). The maximum surface

235   precipitation is slightly shifted upstream relative to the convective updraft (Fig. 5a). The upper-level WCB outflow remains inside a comparatively thick cirrus cloud for several hours, which has formed during the convective ascent and is subsequently advected with the upper-level mean flow (Fig. 5c, purple contours). This convectively formed cirrus cloud can be considered as a longer-lived convective anvil cloud, suggesting that embedded convection is also relevant for the larger-scale upper-level cloud cover. Cloud top height reaches a local maximum directly above the convective updraft and an injection of IWC into

240   the lower (dynamical) stratosphere can be observed, indicating the potential for overshooting convection and moistening of the lower stratosphere with WCBs (Fig. 5c).

The cloud formed during the slantwise WCB ascent is comparatively less dense, with reduced rain, ice, and snow water content and without graupel production (Fig. 5b,d). Accordingly, the cloud structure and cloud top are horizontally more homogeneous and stratiform, and the surface precipitation maximum is substantially weaker compared to the convective WCB

245   ascent (peak value reduced by a factor of 3). The vertically integrated rain, snow and graupel water paths for the slantwise WCB trajectories are substantially lower and distributed homogeneously over a larger area (Fig. 5b). Interestingly, also for the slantwise WCB trajectories, an intrusion of IWC into the stratosphere occurs in the simulation (Fig. 5d). The WCB outflow is surrounded by a cirrus cloud during the entire ascent, indicating the relevance of WCBs for the formation and maintenance of the extended upper-level cirrus cloud cover associated with extratropical cyclones (Eckhardt et al., 2004; Madonna et al., 2014;

250   Oertel et al., 2019; Joos, 2019).

In comparison to the slantwise WCB, the vertically integrated rain, snow and graupel water path in close proximity to the convective updraft is considerably higher (Fig. 5a,b). This leads to a denser cloud (Fig. 5c,d) with limited spatial extent (Fig. 5a,b) in the convective case and implies a pronounced heterogeneity of the large-scale cloud structure if convection is embedded in the large-scale WCB ascent. A previous analysis showed that the precipitating region for the considered cyclone

255 is spatially confined to the WCB ascent region (cf. Oertel et al., 2019, Fig. 9b). Indeed, the (normalized) number of convective and slantwise WCB trajectories correlate both well with the evolution of the averaged (non-zero) precipitation in the WCB domain (Fig. 2b). Nevertheless, both convective ascent pulses clearly coincide with the domain-averaged precipitation maxima, suggesting that the evolution of embedded convection in the WCB has an impact on precipitation intensity (cf. Oertel et al., 2019).

260 The distinctly different cloud and precipitation structure between both WCB trajectory categories underlines the rationale of our classification of convective versus slantwise ascent, and agrees with typical characteristics of both precipitation types: The convective WCB ascent produces locally confined, intense precipitation including the formation of graupel, while the precipitation associated with the slantwise WCB ascent is much less intense and distributed over a larger domain whereby the ascent velocity is too slow for graupel production and leads to a stratiform cloud band.

265 Consistent with the formation of clouds and precipitation, the convective WCB trajectories experience substantial cloud diabatic heating of on average 35 K during the first 3 h and reach their outflow level at around 330 K in agreement with their initial θ_e value. The averaged total cross-isentropic ascent of the slantwise WCB trajectories with lower θ_e in the inflow is weaker with about 28 K in 18 h when their final outflow level is reached at around 323 K. The strong and localized heating in the convective updrafts leads to a local increase of the melting level height (Fig. 5c) and a downward deflection of the isentropes

270 in the diabatically heated region (Fig. 3c and 4e).

Both convective and slantwise WCB trajectories ascend only approximately along constant θ_e surfaces (Fig. 4a,b) due to the influence of microphysical processes during the ascent. The calculation of θ_e only considers the heat released during the transition from the vapour to the liquid phase, but does not account for the additional heat release associated with the ice phase (the transition from the vapour to the ice phase releases the latent heat of condensation plus freezing ($L_c + L_f$), and the latter is

275 not accounted for in the calculation of θ_e). Hence, the influence of melting from falling hydrometeors and the phase transitions to ice above the 0°C isotherm are evident for the WCB ascent. Following the ascent, once the melting level is reached in the vicinity of the 0°C isotherm, i.e., where a transition from the solid (RWC) to the liquid (SWC and GWC) phase occurs (Fig. 5c), θ_e decreases due to melting of snow and graupel falling into the ascending air parcels (Fig. 3c). At higher altitudes, θ_e increases again due to the additional heat release in the ice phase. This process of decrease and subsequent increase of θ_e

280 along the ascent is also evident in the more slowly ascending WCB trajectories (Fig. 3d). This underlines the importance of microphysical processes in WCBs (Joos and Wernli, 2012; Joos and Forbes, 2016), whose effect is clearly detectable even after averaging over hundreds of trajectories. [1]

---

[1]Note that the non-conservation of θ_e leads to the non-conservation of the equivalent potential vorticity (EPV) along the ascent, which is often considered to be conserved (e.g., Hitchman and Rowe, 2017) for saturated convective motion (neglecting PV modification through the solenoid effect; for details see Cao and Cho, 1995). EPV is defined as PV but with θ_e replacing θ (EPV $= \frac{1}{\rho}\boldsymbol{\omega} \cdot \nabla \theta_e$).

3.4 Vertical and horizontal PV structure

The PV perspective is useful to understand and trace the effect of convection on the atmospheric circulation. In this section we
285   investigate the 3D PV structure associated with convective and slantwise WCB ascent and describe the mechanisms that lead
to the observed PV distribution.

    The strong localized diabatic heating during the ascent results in a PV production below and a PV destruction above the
strongest ascent phase for both WCB categories (Fig. 4e,f), which is characteristic for WCB ascent (e.g., Wernli and Davies,
1997; Pomroy and Thorpe, 2000; Madonna et al., 2014). In comparison with the more slowly ascending WCB trajectories,
290   in particular the positive PV anomaly formed by convective WCB ascent is much stronger and more localized. The average
low-level PV anomaly below the convective WCB ascent reaches values of up to 4.5 PVU, while it remains below 1.5 PVU for
the slantwise WCB ascent. In the WCB outflow, the PV values decrease to approximately 0.2 PVU for both WCB categories
(Fig. 4e,f). Despite the stronger and vertically more extended positive low-level PV anomaly produced by the convective WCB
trajectories, both types of WCB trajectories lead to an extended region of low-PV air in the outflow in the upper troposphere. In
295   particular the outflow of the convective WCB trajectories is associated with a region of low static stability ($\mathrm{d}\theta/\mathrm{d}z \leq 2\,\mathrm{K}\,\mathrm{km}^{-1}$,
Fig. 4e, white hatching).

    In the following, we examine the PV structure not only along the ascent, but also in the surroundings of the WCB ascent.
Furthermore, we consider the theoretical concept for PV modification as well as the vorticity and static stability structure within
the PV anomalies.

3.4.1 Low-level positive PV anomaly

Figure 6a shows the PV structure in the lower troposphere below the mean trajectory position 30 minutes after the start of
the convective WCB ascent. There, below the level of the diabatic heating maximum, the convective WCB ascent leads to
the strong positive PV anomaly identified in the along-flow analysis (Fig. 4e). This mesoscale PV monopole with values up
to 4 PVU extends horizontally about 30 km around the convective udpraft and is embedded within an environment with a
305   lower-amplitude positive PV anomaly that results from the slower, slantwise WCB ascent (Fig. 6b). In contrast to the strong
mesoscale PV anomaly formed by the convective WCB ascent, the PV anomaly associated with the slantwise WCB ascent
has a lower magnitude of around 1.5 PVU. However, the PV anomaly occurs on a larger spatial scale of up to 100 km, with
decreasing amplitude away from the WCB ascent. Hence, due to the stronger and more localised diabatic heating in the
convective WCB trajectories (cf. section 3.3), and, as a consequence, stronger PV modification, the mesoscale PV anomaly
310   produced by convection is superimposed on and embedded in the PV signal resulting from the larger-scale and slower WCB
ascent (Figs. 6a,b).

3.4.2 Upper-level PV dipole

In the middle to upper troposphere a coherent mesoscale horizontal PV dipole forms in the vicinity of the convective WCB
trajectories, with a positive PV anomaly of magnitude 3 PVU to the right of the thermal wind vector and a negative PV anomaly

of magnitude -1.5 PVU to the left of the thermal wind vector (Fig. 6c,e). This PV dipole extends vertically from about 3 km (305 K) to about 9 km (330 K). The maximum amplitude of the PV dipole occurs at about 315-320 K (Fig. 6e) and coincides with the diabatic heating maximum associated with the formation of snow and graupel (Fig. 5c). Similar to the positive PV monopole at low levels, the upper-level PV dipole also extends to about 30-40 km around the center of the convective updraft (Fig. 6c).

This distinct mesoscale PV signal emphasizes the coherent signature of the individual convective updrafts that are embedded within the complex WCB airstream. The robust mesoscale response can only be identified so clearly in the composite analysis. The small-scale and fragmentary PV features that occur in the upper troposphere in the region of embedded convection on instantaneous PV charts (Fig. 8d, cf. Oertel et al., 2019, Fig. A1) correspond to such mesoscale PV dipoles formed by the individual convective updrafts embedded in the WCB.

The formation of the PV dipole above the low-level PV monopole in our composite analysis is directly comparable to the PV structure of isolated convective updrafts in a sheared environment (cf. Chagnon and Gray, 2009) or larger-scale convective systems as discussed in the introduction. It has, however, not yet been associated with WCBs identified in reanalysis data and coarser-scale simulations, where the vertical PV dipole structure dominates (e.g., Wernli and Davies, 1997; Joos and Wernli, 2012; Madonna et al., 2014).

The composites for the slantwise WCB trajectories reveal the typical PV structure of WCBs (e.g., Wernli and Davies, 1997; Pomroy and Thorpe, 2000) with a wide region of low-PV air with a magnitude of about 0.5 PVU in the upper-tropospheric WCB outflow above the low-level positive PV anomaly (Fig. 6b,d,f and 4f). The poleward ascending low-PV air in the WCB outflow spreads out into the upper tropospheric ridge, potentially leading to its amplification (Grams et al., 2011; Madonna et al., 2014).

3.4.3 Mechanisms leading to the PV structure

We now analyse the mechanisms responsible for the formation of these coherent PV anomalies. To do so, we consider the material change of PV in the form of Eq. 4, which emphasizes the contributions from the vertical (first term) and horizontal (second term) vorticity components and heating gradients.

The formation of the low-level positive PV anomaly is mainly due to the strong vertical heating gradient in an environment with large cyclonic vertical vorticity (first term in Eq. 4), such that below the diabatic heating maximum PV is increased (e.g., Stoelinga, 1996; Wernli and Davies, 1997; Rossa et al., 2000; Joos and Wernli, 2012; Binder et al., 2016). This mechanism is important for PV modification in both the convective and slantwise WCB trajectories, which ascend near the surface cold front, i.e., in a region where absolute vertical vorticity $f + \zeta$ is particularly large. Due to the stronger and more localised diabatic heating in the convective WCB ascent, the vertical heating gradient $\frac{\partial \dot{\theta}}{\partial z}$ is larger and, therefore, the convective WCB ascent leads to a stronger low-level positive PV anomaly. Furthermore, vortex stretching in the convective updraft additionally enhances the low-level absolute vertical vorticity (Fig. 7a). Together, this can lead to a positive feedback mechanism: PV is diabatically produced in the convective updraft with strong diabatic heating gradients $\frac{\partial \dot{\theta}}{\partial z}$. In consequence, the vertical vorticity is enhanced supported by vortex stretching. In the following, the diabatic heating gradient acts on amplified vertical vorticity,

and thus still larger PV anomalies are produced. Finally, this results in increased PV production (cf. Joos and Wernli, 2012;
350 Madonna et al., 2014).

The mid- to upper-level convective PV dipole results from the arrangement of horizontal vorticity and the horizontal diabatic
heating gradient (second term in Eq. 4, Fig. 1). Horizontal vorticity is large ahead of the upper-level trough due to strong vertical
wind shear below the upper-level jet. The horizontal vorticity vector $\boldsymbol{\omega}_\mathrm{h}$ is rotated 90° anticlockwise relative to the thermal
wind vector and points towards the cold air. Moreover, the horizontal heating gradients $\nabla_\mathrm{h}\dot\theta$ point radially towards the center
355 of the convective updraft. This results in PV production to the right of the thermal wind vector, where $\nabla_\mathrm{h}\dot\theta \parallel \boldsymbol{\omega}_\mathrm{h}$, and PV
destruction to the left of the thermal wind vector, where $\nabla_\mathrm{h}\dot\theta \parallel -\boldsymbol{\omega}_\mathrm{h}$. The convectively produced heating gradients and the
background vorticity are strong enough to form a region of absolutely negative PV. These findings from the WCB composites
agree with the theoretical considerations in the introduction.

The horizontal diabatic heating gradients for the slantwise WCB ascent are weaker because the diabatic heating is (i) less
360 intense and (ii) spatially more uniform due to a larger-scale gradual ascent (cf. Fig. 3b,d). Thus, the vertical component of the
PV equation dominates for the slantwise WCB ascent (first term in Eq. 4), where continuous heating along the ascent leads
to PV reduction above and a transport of low-PV air to the upper troposphere by the trajectories passing through this low-PV
region. However, PV values remain positive because PV cannot change sign if the first term in Eq. 4 dominates. We conclude
that for the slantwise WCB ascent the vertical component of the PV equation is most relevant, while for embedded convection
365 with localised and intense heating gradients the horizontal components of the PV equation are essential to explain the resulting
upper-level PV dipole structure.

3.4.4 Partitioning of PV anomalies in vorticity and static stability

Negative PV implies either hydrostatic, inertial or symmetric instablility (e.g., Schultz and Schumacher, 1999; Hoskins, 2015).
In the following, we analyse the partitioning of the PV anomalies in vorticity and static stability and discuss its implication for
370 the expected lifetime of these anomalies. Figure 7b shows that the PV dipole is associated with a dipole of vertical vorticity with
similar magnitude in both poles, and thus, can be understood as the effect of tilting of horizontal vorticity by the convective
updraft. Moreover, strong heating in the convective updraft leads to increased static stability inside the updraft ($\mathrm{d}\theta/\mathrm{d}z =
3-5\,\mathrm{K\,km^{-1}}$; not shown) and a shallow layer of low static stability ($\mathrm{d}\theta/\mathrm{d}z \leq 2\,\mathrm{K\,km^{-1}}$, Figs. 4e and 6e) above. Note that
static stability is relatively uniform across both poles. Hence, the PV dipole's horizontal structure is predominantly determined
375 by vorticity and not static stability. This is consistent with Chagnon and Gray (2009), who also found that in convective
updrafts the so-called 'latent vorticity' is quickly converted to horizontal dipoles of vertical vorticity that determine the PV
dipole structure.

In section 5 we will see that the negative PV pole, produced by convective WCB trajectories, persists for several hours. This
is consistent with adjustment timescales of several hours (e.g., Thompson et al., 2018) in inertially unstable regions where
380 $f + \zeta < 0$. A convectively unstable atmosphere ($\mathrm{d}\theta/\mathrm{d}z < 0$), in contrast, would adjust to stability on a timescale of less than
1 h (Schultz and Schumacher, 1999).

For both WCB categories static stability is reduced in the upper troposphere near the WCB outflow (Fig. 6e,f, white hatching). The static stability reduction above the convective WCB is stronger (Fig. 6e), but the slantwise WCB leads to a reduced static stability over a larger region (Fig. 6f). In the outflow of the slantwise WCB relative vorticity is weakly negative and absolute vertical vorticity is weakly positive (not shown).

The low-level positive PV anomalies for convective and slantwise WCB ascent are associated with large cyclonic vertical vorticity $f + \zeta$, whereby the convective WCB has higher values, exceeding $6 \cdot 10^{-4}\,\mathrm{s}^{-1}$ (Fig. 7a), compared to the slantwise WCB with values of $(3 - 4) \cdot 10^{-4}\,\mathrm{s}^{-1}$ (not shown).

3.5 Flow anomalies induced by PV anomalies

In agreement with idealized PV inversions (e.g., Hoskins et al., 1985; Hoskins, 2015), where a positive/negative PV anomaly induces a cyclonic/anticyclonic flow anomaly, the convectively produced PV anomalies are associated with coherent horizontal wind anomalies, calculated as the deviation of the current wind vectors from the 2-h centered mean wind vectors. The low-level positive PV anomaly is accompanied by a cyclonic circulation anomaly with about $4\,\mathrm{m\,s}^{-1}$ higher wind speeds southeast of the convective updraft and smaller values to the northeast (Fig. 6a,e). Despite this relatively strong local wind anomaly, its radius of impact is limited and the effect of the PV anomaly substantially decays beyond 40 km from the updraft. As hypothesized by Raymond and Jiang (1990), the relatively long-lived low-level positive PV anomalies interact with the background shear, and thus could trigger new convective cells through the formation of local convergence lines on the downshear side. In this way convective activity is maintained.

The positive PV monopole from the slantwise WCB trajectories also induces a cyclonic low-level circulation anomaly (Fig. 6b). Yet, it hardly exceeds $1\,\mathrm{m\,s}^{-1}$ and occurs on a larger spatial scale, in agreement with the comparatively weaker and larger-scale positive PV anomaly. The initial slantwise WCB ascent occurs directly behind the pronounced low-level jet ahead of the cold front (Fig. 6b,f). This jet, which exceeds $24\,\mathrm{m\,s}^{-1}$, is accelerated by the diabatically produced positive PV and the associated cyclonic circulation anomaly ahead of the WCB ascent region. This pattern agrees with the synoptic situation of early WCB studies (e.g., Wernli, 1997, Fig. 5), where the ascent region of the slantwise WCB is located ahead of the upper-level jet and behind the low-level jet.

The convectively produced upper-level PV dipoles are associated with a cyclonic and anticyclonic circulation anomaly around the positive and negative PV poles, respectively (Fig. 6c,e). The superposition of these two flows leads to a deceleration of the flow in the center of the PV dipoles and potentially stabilizes the convection against rapid propagation with the upper-level flow. At 320 K, this induced wind anomaly reaches almost $3\,\mathrm{m\,s}^{-1}$ close to the convective updraft.

The weaker negative upper-level PV anomaly of the more slowly ascending WCB trajectories has a widespread weak anticyclonic circulation anomaly (Fig. 6d) with a maximum anticyclonic wind speed anomaly of less than $0.5\,\mathrm{m\,s}^{-1}$ northwest of the WCB ascent. The more slowly ascending WCB trajectories arrive in the upper troposphere in the vicinity of the tropopause.

In summary, both WCB categories are associated with a cyclonic low-level circulation anomaly induced by the low-level positive PV anomaly. The wind anomaly in the convective case is stronger but the extent is limited, while the wind anomaly in the slantwise WCB category is substantially weaker but extends to a larger region. In the upper troposphere two different

circulation anomalies establish. The slantwise WCB ascent induces a widespread and comparatively weak anticyclonic circulation anomaly. In contrast, the anticyclonic and cyclonic circulation anomalies induced by the convectively generated PV dipole occur on a smaller scale and lead to a deceleration of the flow in the center of the convective updraft.

4 An illustrative example of WCB-embedded convection

420 Figure 8 shows an instantaneous example of convection embedded in the large-scale WCB cloud structure and serves to illustrate the typical properties and characteristics deduced from the composites analysis in the real synoptic context. The large-scale WCB cloud band (Fig. 8a) is heterogeneously structured with a strong and localised production of graupel, snow and rain (Figs. 8b and 9a) produced by enhanced updrafts from embedded convection. Embedded convection, identified by rapidly ascending WCB trajectories (Fig. 8c, white contours), is predominantly located in the baroclinic region ahead of the upper-level

425 trough (Fig. 8a and 8c, white contours). Indeed, the online trajectories' ability to identify the convective ascent is confirmed by the vertical cross-section through an embedded convective updraft (Fig. 9a): A substantial amount of hydrometeors is locally produced inside the convective updraft. This spatial coincidence of pronounced hydrometeor production within the updrafts (compare Figs. 8b, c and Fig. 9a) agrees with the results from the composite analysis (Fig. 5a,c) and emphasizes the heterogeneous cloud structure arising from WCB-embedded convection (Fig. 8b).

430 Although the upper-level PV associated with the convective updrafts is fragmented into many small-scale features (Fig. 8d), the PV structure identified in the composite analysis (cf. Fig. 6e) is clearly discernible in a vertical cross-section through the convective updraft (Fig. 9b): in the lower troposphere a strong positive PV monopole forms, which is replaced by a horizontal PV dipole centered around the convective updraft in the mid- to upper troposphere. The PV dipole extends from around 4 km to 11 km height and the PV anomalies exceed ± 10 PVU, leading to large PV gradients of up to $1\,\mathrm{PVU\,km^{-1}}$.

435 In agreement with the composite analysis, the static stability at the height of maximum diabatic heating at around 320 K is increased (not shown), while above the heating maximum a lense of low static stability forms across the negative and positive PV poles (Fig. 9b, white contour and hatching). Thus, the mesoscale PV dipole pattern originates predominantly from the spatial variability of vertical vorticity.

The composite analysis (section 3.2) revealed that the convective WCB trajectories ascend in a region characterized by sub-

440 stantially higher θ_e that forms a narrow elongated tongue of warm and moist air ahead of the cold front. Figure 8e emphasizes the strong heterogeneity of θ_e in the warm sector and confirms the spatial coincidence of rapid WCB ascent (Fig. 8e, white contours) and the localised narrow structures of high θ_e air. This underlines the role of the mesoscale temperature and humidity gradients for triggering convection that is directly embedded within the large-scale slantwise WCB ascent.

In the lower troposphere an elongated zone of horizontal wind convergence concurs with the convective updraft region

445 (Fig. 8f). This low-level convergence line coincides with a band of increased low-level PV (Fig. 8f, contour lines), which are generated and further enhanced by convective ascent (cf. section 3.4).

On the larger-scale (after a coarse-graining of the PV field to a $60\,\mathrm{x}\,60\,\mathrm{km^2}$ grid, see section 5), the convective region forms a meridionally elongated and narrow upper-level PV dipole band with an extension of $100\,\mathrm{km}$ in the across-front and more

than 400 km in the along-front direction, respectively (Fig. 8c). The orientation of this dipole band is aligned with the thermal
450 wind vector. Hence, despite the small-scale noise in the PV field formed by the individual convective updrafts (Fig. 8d), the PV
anomalies spatially aggregate to a coherent and robust PV structure on the larger scale (Fig. 8c). The formation of this elongated
PV dipole parallel to the convective region is consistent with the composite analysis (Fig. 6c) and theoretical considerations
(cf. Eq. 4 and Fig. 1).

A larger-scale circulation anomaly establishes around the coarse-grained PV dipole band with cyclonic and anticyclonic
455 wind anomalies around the positive and negative poles, respectively (Fig. 8c). The wind anomalies scale with the amplitude
of the PV anomalies and are particularly strong in the region where the coarse-grained PV anomalies exceed ± 2 PVU. Note
that the wind anomalies are not coarse-grained, emphasizing that the organized mesoscale PV features aggregate to coherent
PV anomalies on the large-scale, which are directly associated with a dynamical response on the large-scale. This agrees with
the electrostatics analogy of PV (Bishop and Thorpe, 1994), which suggests that locally confined PV 'charges' each induce a
460 certain far-field effect on the flow and the superposition can be attributed to the spatially integrated PV anomaly. This implies
that the linear superposition principle is applicable to PV, which denotes that the effects of individual PV anomalies on the flow
field are additive (Bishop and Thorpe, 1994; Birkett and Thorpe, 1997). Although the linear superposition is only exactly valid
for quasi-geostrophic PV, Thorpe and Bishop (1995) and Birkett and Thorpe (1997) suggested that the non-linear contributions
for Ertel PV decrease with distance and with decreasing amplitude of the PV anomaly, and can therefore likely be neglected.
465 This study supports their conclusion because the convective PV anomalies aggregate to coherent larger-scale PV anomalies
with a distinct effect on the flow field.

The associated circulation anomaly leads to an increase of the wind speed to the northwest and southeast of the negative and
positive pole, respectively, and to a deceleration of the flow in the PV dipole's center (Fig. 8c,d). Although the far-field effect
of the PV anomalies reaches beyond the region where PV is directly modified, the upper-level waveguide is located more than
470 250 km to the west of the convective band and, therefore, at this particular time when convection forms the PV dipole, the
circulation anomaly does not yet directly influence the upper-level waveguide.

In summary, this instantaneous, Eulerian analysis of WCB-embedded convection agrees with the composite analysis in
section 3 and illustrates the typical properties of WCB-embedded convection: strong and localised diabatic heating inside a
dense and precipitating cloud leads to the formation of mesoscale upper-level PV dipoles that are associated with a coherent
475 larger-scale circulation anomaly.

5 PV anomalies on a larger scale and relevance for large-scale dynamics

Whereas section 3 showed that the individual convective updrafts are associated with mesoscale upper-level PV dipoles that
are, however, too small-scale to directly interact with the synoptic-scale balanced flow (cf. Shutts, 2017), section 4 illustrated
that these fragmentary PV anomalies can indeed aggregate to larger-scale PV dipole bands. In the following, we assess the
480 potential for the interaction of these convectively produced PV dipole bands with the synoptic-scale flow. For this, the PV field
is spatially averaged using a 60-km smoothing radius (cf. Shutts, 2017; Clarke et al., 2019). More specifically, we project the

original 2 km PV field to a coarser grid using a spatial moving average over 60 x 60 km^2. This PV coarse-graining is performed on selected isentropes and results in a smoothed isentropic PV field with an effective resolution of 60 km.

The coarse-graining emphasizes the coherent larger-scale PV anomalies associated with the convective regions (cf. section 4
485   and Figs. 8c,d). They take the form of elongated PV dipole bands (400 x 100 km) aligned with the elongated narrow band of convective activity ahead of the cold front (Figs. 8c,d and 10a), in agreement with the PV dipole composite analysis in section 3.4. We now investigate how these PV dipole bands evolve in time and whether they interact with the large-scale PV waveguide.

5.1   Temporal evolution of convectively generated upper-level PV dipoles

490   At the time when the PV dipole bands are formed, the associated circulation anomalies do not reach to the upper-level waveguide and jet stream (Figs. 8c and 10a). The negative PV band is located 250 km east of the upper-level trough, and the induced wind anomalies are confined to within about 100 km, and hence, do not directly interact with the waveguide. Yet, the temporal evolution reveals that, even after the convective updrafts cease, the negative PV band persists (Fig. 10a-d): During its relatively long lifetime of several hours, the negative PV pole is advected by the upper-level wind to the north and toward the dynamical
495   tropopause. The negative PV appears to be approximately conserved and, a couple of hours after the convective updraft ceased, the negative PV band has approached the upper-level jet (distance now only around 150 km) and the adjacent wind speed at the jet has increased by approximately 5 ms^{-1} to more than 60 ms^{-1} (Fig. 10c). To confirm the advection of the negative-PV air by the upper-level flow, forward trajectories are started inside the negative PV anomaly at the time when the PV dipole band is formed by the embedded convection (Fig. 10a, pink shading; for more details about the trajectory computation see below):
500   The positions of these forward trajectories (Fig. 10a-d, pink shading) mostly coincide with a negative PV region, in particular within the first 3-6 h.

After 9 hours, the negative PV pole, distorted in shape due to the influence of strong horizontal wind shear in the jet region, closely approaches the waveguide and thereby strongly increases the isentropic PV gradient near the tropopause (Fig. 10d-e). The strong anticyclonic circulation anomaly associated with the negative PV anomaly accelerates the jet and forms a local jet
505   streak (Figs. 10d,e) that is maintained for 2-3 h. This local jet intensification occurs although during advection of the negative PV anomaly, its magnitude decreases (Fig. 10f) compared to the initial strength immediately after its formation (Fig. 9b). The area covered by negative PV values, on the other hand, increases on the considered isentrope (Figs. 10a-d, blue contours). This negative PV anomaly in the ridge ahead of the upper-level trough appears to amplify the amplitude of the pre-existing PV pattern at the waveguide.
510   With time, the negative PV pole overtakes the positive PV pole (Fig. 10a-d, orange and red contours) due to strong horizontal wind shear, i.e., decreasing upper-level wind with increasing distance to the jet. In contrast to the negative PV pole that is advected towards the waveguide, the positive PV anomaly remains in the ridge and away from the waveguide.

5.2 Analysis of trajectories initialized at 09 UTC 23 Sep

The origin and fate of the negative PV air is analysed in more detail using offline trajectories with 15-minute temporal resolu-
515   tion. For this, forward and backward trajectories were computed from a region of convectively produced negative PV (Fig. 10a,
pink shading). We only selected trajectories with negative PV between 315 K and 325 K that are located within a larger region
of spatially averaged negative PV at 09 UTC 23 Sep. At this time, which we will refer to as $t=0$ h, all trajectories have negative
PV values and are located in a larger region of negative PV (Figs. 10a and 11a).

With the backward trajectories we can infer when, relative to $t=0$ h, the negative PV air masses acquired their negative PV
520   and where they originate from (Fig. 11). Six hours before, less than 10% of these trajectories have negative PV, while 3 h before
this percentage amounts to 30% (Fig. 11b, black curve). At $t=-1$ h more than 40% of trajectories gain a negative PV value as
they pass through a convectively influenced region (not shown), resulting in PV destruction to the left of the thermal wind
vector and the convective updraft. Thus, the majority of trajectories acquires their negative PV just within the last hour while
passing a convectively influenced region.

525   From all trajectories with negative PV at $t=0$ h, almost 70% were previously advected quasi-isentropically with the upper-
level flow and a smaller percentage of 30% ascended from the lower to mid-troposphere (Fig. 11b, grey curves and Fig. 11c),
some of them inside a convective region. The percentage of upper-level trajectories with negative PV advected into the negative-
PV region increases with time (Fig. 11b, solid blue curve) because upstream convection produced negative upper-level PV
1-3 h earlier (not shown). This air mass is then advected and contributes to the larger-scale region of negative PV at $t=0$ h. The
530   strongest increase of the percentage of upper-level trajectories with a negative PV value occurs at $t=-1$ h (Fig. 11b, solid blue
curve), when strong convection sets in and modifies the PV of the trajectories to the left of the convective updraft. Trajectories
that ascend from lower levels (Fig. 11c) and contribute to the larger-scale region of negative PV at $t=0$ h have PV values of
± 10 PVU (Fig. 11a). However, the percentage of trajectories with negative PV ascending from the lower troposphere is small
and does not exceed 10% (Fig. 11b, dashed blue curve).

535   These results suggest that the larger-scale region of upper-level negative PV consists of air masses with different origins:
(i) a large percentage of trajectories (approximately 30%) with negative PV is formed by upstream convection approximately
3 h earlier and is advected quasi-isentropically by the upper-level flow; (ii) a substantial fraction of air parcels (approximately
40%) originating from the upper troposphere gains negative PV only within the last 1 h through local convective influence as
they pass the left side of a convective updraft; (iii) only a small fraction of trajectories contributing to the upper-level negative
540   PV at $t=0$ h originates from the lower to mid-troposphere with positive PV, whereby these rising trajectories gain a negative
PV value during their ascent or after arrival in the upper troposphere when they pass through a convectively influenced region;
(iv) the smallest fraction of less than 10% contains trajectories that ascend from lower levels with already negative PV 3 h prior
to their ascent.

Although there is some uncertainty in the calculation of the offline trajectories with 15-minutes temporal resolution, these
545   results suggest that air masses that gain negative PV originate from a region in close proximity to convection but not necessarily

from inside the convective updraft. Moreover, this indicates that the maintenance of convective ascent for at least a few hours helps to generate a larger region of negative PV through advection of negative PV from upstream convection.

Whereas the backward trajectories allowed analysing the PV history of the air parcels, the forward trajectories consider the future evolution of their PV. Within the first 3-6 h the forward trajectories remain mostly within a negative PV region (Fig. 10a-d, pink shading) and the majority of trajectories keep their negative PV values (Fig. 11a). This emphasizes the persistence of the negative PV and supports the previous finding that the negative PV region is advected by the upper-level flow (Fig. 10). After 6 h the trajectories spread out spatially and cover a larger region due to the strong horizontal and vertical wind shear, but 57% of the trajectories still have negative PV. The negative PV is retained for a relatively long time, and even after more than 12 h more than 50% of all trajectories still have negative PV (Fig. 11a) and contribute to some extent to a widespread larger-scale negative PV anomaly (Fig. 10d-e, pink shading), which induces an anticyclonic circulation anomaly in proximity to the tropopause.

Together these results suggest that air masses in the vicinity of convective updrafts experience strong PV destruction, which contributes to a larger region of negative PV with a coherent anticyclonic circulation anomaly. The convectively generated negative PV is characterised by a relatively long lifetime and is advected northward towards the upper-level jet, where it interacts with the upper-level waveguide, strengthens the isentropic PV gradient and is associated with the formation of a jet streak.

5.3 Convectively generated low-level positive PV anomalies

The convectively generated positive PV anomalies in the lower troposphere are characterized by a high amplitude of up to 10 PVU, and form an elongated narrow region (not shown). The spatial scale of these low-level PV anomalies is overall smaller than the upper-level PV anomalies (compare Fig. 8d and f), and after coarse-graining to 60 km the PV anomaly is smeared out and its amplitude strongly decreases to approximately 1.5-2 PVU (not shown). If a coarse-graining to 12 km is applied instead, a narrow and elongated PV band with magnitude exceeding 2-5 PVU is found (Fig. 8f). The convectively generated PV bands frequently coincide with low-level convergence lines (Fig. 8f) and are also characterized by a comparatively long lifetime. Thus, before these low-level PV stripes slowly decay, they also propagate poleward (not shown), where the induced cyclonic circulation anomaly can potentially enhance the low-level jet downstream.

6 Discussion and open question

In the following we discuss our results and remaining open questions about the significance of embedded convection in WCBs. In this WCB case study, embedded convection was frequently observed and consistently associated with elongated upper-level PV dipole bands, whereby the negative PV pole was advected poleward towards the jet where it interacted with the waveguide. However, the analysis of only one case study limits the generality of the key results, i.e., the frequent occurrence of convectively produced PV dipole bands in WCBs. But despite the large variability of WCB ascent behaviour, we hypothesize that the WCB ascent regions are generally favorable environments for the production of PV dipole bands and the occurrence of negative

PV in proximity to the tropopause. While observations of negative PV in ridges of mid-latitude cyclones in proximity to the tropopause have already been reported (e.g., Pomroy and Thorpe, 2000; Grams et al., 2011; Chagnon et al., 2013; Rowe and

580   Hitchman, 2016), it has not yet been explicitly associated with embedded convection in WCBs. The extension of this analysis to further WCB case studies – including the investigation of embedded convection, its PV signature and its dynamical relevance – would shed light on the generality of our key results. In particular, the identified impact of embedded convection on the dynamics and precipitation pattern requires a climatological quantification of the frequency of convective versus slantwise WCB ascent. However, the investigation of numerous WCB case studies in convection-resolving models is computationally

585   expensive, also because of the large domain covered by the WCB and the inclusion of online trajectories.

    In addition to the increase of the tropopause sharpness by WCBs (Chagnon et al., 2013; Chagnon and Gray, 2015), the advection of the convectively generated negative PV pole towards the waveguide further enhances the horizontal PV gradient in proximity to the tropopause. This locally accelerates the jet and potentially influences the propagation of Rossby waves (Harvey et al., 2016), both highly relevant aspects for NWP. During its poleward advection towards the tropopause, the negative PV

590   pole wraps anticyclonically due to the strong wind shear near the jet and expands in the ridge (cf. Chagnon et al., 2013). This expansion increases the influence of PV on the induced velocity, as larger-scale PV anomalies more strongly affect the velocity field. Moreover, this stresses that, although embedded convection locally strongly impacts the precipitation, cloud structure, and the mesoscale flow during the convective updraft, the impact on the large-scale dynamics occurs mostly downstream and several hours after the convective updraft ceases.

595   A study of an extratropical cyclone by Chagnon et al. (2013) showed that diabatic processes do not necessarily alter the PV directly at the tropopause, but that PV in its proximity is diabatically modified, resulting in the steepening of the PV gradient across the tropopause. They showed that negative PV had been diabatically modified within the WCB outflow on the equatorward side of the trough, and subsequently stretched out in the ridge through non-linear advection, similarly to the behaviour of the convectively generated negative PV during poleward advection into the ridge in this case study (section 5,

600   Fig. 10). In their case study, the negative diabatic PV, resulting from parameterized convection, large-scale microphysical processes and boundary layer processes, was in phase with the meridional PV gradient, which resulted in the amplification of the wave amplitude, and thus was associated with faster Rossby wave growth rates and westward propagation. Similarly, the negative PV band formed by WCB-embedded convection, located in proximity to the tropopause, is in phase with the meridional PV gradient, and thus, also enhances the wave amplitude and steepens the PV gradient.

605   Currently, global forecast models (e.g., IFS, MetUM, GFS) are run with a coarser resolution unable to explicitly resolve convection. This leads to the questions if these schemes are able to trigger embedded convection at the right place and time and with the correct amplitude, and if the PV dipoles generated by localized parameterized heating have the correct magnitude. For instance, previous studies showed that the PV anomaly's amplitude generated by the convection scheme is weaker compared to the amplitude in high-resolution convection-resolving simulations (Done et al., 2006; Clarke et al., 2019), which, in the case

610   of a large mesoscale convective system, subsequently influenced the downstream flow evolution and decreased the forecast quality (Clarke et al., 2019). To explicitly simulate the mesoscale upper-level PV dipoles, a horizontal resolution of at least 10 km would be required to resolve the convective updrafts.

While embedded convection is directly relevant for NWP due to its potential impact on surface precipitation, mesoscale winds, jet speed and Rossby wave propagation, the relevance of correctly representing embedded convection in climate simulations is less obvious. Nevertheless, the misrepresentation of embedded convection in WCBs could underestimate the projected surface precipitation extremes associated with extratropical cyclones. Moreover, the large-scale cloud band of WCBs is known to modify the radiative balance (Joos, 2019), which is still a highly uncertain process in climate simulations (e.g., Boucher et al., 2013; Vial et al., 2013; Bony et al., 2015; Caldwell et al., 2016). A systematic underestimation of embedded convection and its influence on the cloud structure could potentially influence the radiative balance, because, on the one hand, convection results in a substantially denser cloud band. On the other hand, convectively generated liquid-origin cirrus clouds (cf. Krämer et al., 2016; Luebke et al., 2016; Wernli et al., 2016) spread out in the WCB outflow and travel poleward. The formation pathway of cirrus clouds leads to different microphysical and macrophysical properties (e.g., Krämer et al., 2016; Luebke et al., 2016), which can influence the cirrus cloud radiative forcing (Zhang et al., 1999; Joos et al., 2014).

We showed that the formation of the PV dipole through embedded convection is a relatively fast processes, while the decay of the (dynamically unstable) negative PV pole, with a lifetime of several hours, is comparatively slow. It is not yet clear which non-conservative processes, e.g., turbulence, microphysics or radiation, lead to the destruction of the negative PV in the ridge, i.e., the production of PV in regions of negative PV. A novel diagnostic to analyse the PV tendencies from each parameterization scheme available for the ECMWF's Integrated Forecasting System (Spreitzer et al., 2019; Attinger et al., 2019) would enable a detailed and systematic analysis of the processes that govern the destruction of negative PV, and would potentially shed more light on the approximate lifetime and properties of the negative PV in the upper-level ridge.

7 Conclusions

We analysed the effects of embedded convection in the WCB of the North Atlantic cyclone "Vladiana" in Sep 2016 on the precipitation and cloud structure, and on the mesoscale dynamics and circulation features. For this, two categories of online WCB trajectories, very rapidly ascending "convective" WCB trajectories and more slowly ascending "slantwise" WCB trajectories, were identified in a convection-permitting COSMO simulation, and their impact was investigated in a composite analysis and, in more detail for a representative example. As expected from previous studies, the slantwise WCB ascent influences the large-scale precipitation pattern, the hydrometeor and PV distribution in a wide region. The specific signatures of embedded convection are superimposed on these larger-scale pattern from the slantwise WCB ascent. Based on the composite analysis and the investigation of a representative example of embedded convection in the WCB we conclude the following:

The convective WCB trajectories originate from a region with higher θ_e and increased potential instability ($\mathrm{d}\theta_e/\mathrm{d}z$) at approximately 900 hPa compared to their environment, which allows for the rapid quasi-vertical convective ascent through the whole troposphere. Although convective WCB ascent is embedded within the larger-scale region of slantwise WCB ascent, mesoscale θ_e variability and strong localised θ_e gradients in the warm sector give rise to the higher initial θ_e of the convective compared to the slantwise WCB trajectories, which subsequently leads to the more intense cloud diabatic processes and the stronger cross-isentropic ascent (cf. section 1 question 1).

Convective WCB ascent leads to substantially stronger surface precipitation during the ascent with on average more than twice the intensity compared to the slantwise WCB ascent (cf. Oertel et al., 2019). The occurrence of embedded convection is, therefore, relevant for the mesoscale precipitation pattern in cyclones and for extreme surface precipitation associated with WCBs (Pfahl et al., 2014). Moreover, the strong convective updrafts allow for graupel formation, which is absent in the
650 slantwise WCB ascent. Likewise, convective WCB ascent leads to a denser cloud structure in the convective updraft that is embedded within a larger-scale and less dense cloud band (cf. section 1 question 2).

Convective WCB ascent leads to stronger low-level positive PV anomalies along the ascent compared to the slantwise and more slowly ascending WCB trajectories. The convective WCB ascent results in the formation of mid- to upper-level horizontal PV dipoles on both sides of the convective updraft, where the negative pole (with a diameter of approximately 30 km) occurs
655 to the left of the thermal wind vector, i.e., relatively close to the upper-level jet (cf. section 1 question 3). The maximum amplitude of the PV dipole at around 315-320 K coincides approximately with the diabatic heating maximum associated with snow and graupel formation. These convectively produced PV anomalies are predominantly anomalies of absolute vertical vorticity. Static stability inside the convective updraft and in both poles is slightly increased compared to the environment due to strong latent heat release in the updraft. Above the updraft, at about 10 km height, a shallow region of low static stability
660 inside a cirrus cloud spreads out horizontally.

The low-level and upper-level mesocale PV anomalies of the convective WCB trajectories are associated with a coherent circulation anomaly, indicating that PV invertibility is qualitatively also valid at this scale. The positive low-level PV monopole below the convective updraft center induces a cyclonic wind anomaly resulting in a local increase (decrease) of the low-level wind velocity to the right (left) of the thermal wind vector. The upper-level PV dipole is associated with cyclonic and anti-
665 cyclonic circulation anomalies around the positive and negative poles, respectively. The superposition of these PV anomalies leads to a deceleration of the flow near the convective updraft and potentially stabilizes the convectively generated PV dipole against the background flow (cf. section 1 question 4).

On the larger-scale, the individual mesoscale PV anomalies can aggregate to elongated PV dipole bands downstream of the convective updraft region, which are associated with coherent larger-scale circulation anomalies. The negative PV pole is
670 characterized by a relatively long lifetime of several hours. During its lifetime it is advected close to the upper-level waveguide, where it strengthens the isentropic PV gradient. Its anticyclonic circulation anomaly can contribute to the formation of a jet streak more than 1300 km downstream of the convective updraft and the initial formation of the PV dipole. This suggests that the mesoscale PV anomalies produced by embedded convection upstream can influence the synoptic-scale circulation, and are thus dynamically relevant (cf. section 1 question 5).
675 Finally, our mesoscale view on the WCB reveals its heterogeneity and the distinction between slantwise and convective WCB trajectories emphasizes the significantly different impacts on the cloud and precipitation structure and the dynamics, whereby the convective WCB trajectories are accountable for distinct properties, such as the formation of graupel and an upper-level PV dipole, which are absent for purely slantwise ascending WCB trajectories.

Data availability. All data are available from the authors upon request.

680 *Author contributions.* AO performed the simulation and the data analysis, and prepared a first version of the paper. All authors continuously discussed the results and contributed to the final manuscript.

Competing interests. The authors declare that they have no conflict of interest.

Acknowledgements. AO and MB acknowledge funding by the Swiss National Science Foundation (Project 165941). The COSMO simulations were performed at the Swiss National Supercomputing Centre (CSCS), as part of the project sm08 (2017–2019). We appreciate the
685 data from EUMETSAT for the visualization of the WCB cloud band and would like to thank Annette K. Miltenberger for her support with the COSMO online trajectory module.

References

Agustì-Panareda, A., Gray, S. L., and Methven, J.: Numerical modeling study of boundary-layer ventilation by a cold front over Europe, J. Geophys. Res. Atmos., 110, D18 304, https://doi.org/10.1029/2004JD005555, 2005.

690 Anthes, R. A., Kuo, Y.-H., and Gyakum, J. R.: Numerical simulations of a case of explosive marine cyclogenesis, Mon. Wea. Rev., 111, 1174–1188, https://doi.org/10.1175/1520-0493(1983)111<1174:NSOACO>2.0.CO;2, 1983.

Attinger, R., Spreitzer, E., Boettcher, M., Forbes, R., Wernli, H., and Joos, H.: Quantifying the role of individual diabatic processes for the formation of PV anomalies in a North Pacific cyclone, Q. J. R. Meteorol. Soc., 145, https://doi.org/10.1002/qj.3573, 2019.

Baldauf, M., Seifert, A., Förstner, J., Majewski, D., Raschendorfer, M., and Reinhardt, T.: Operational convective-scale numerical weather
695 prediction with the COSMO model: Description and sensitivities, Mon. Wea. Rev., 139, 3887–3905, https://doi.org/10.1175/MWR-D-10-05013.1, 2011.

Ban, N., Schmidli, J., and Schär, C.: Evaluation of the convection-resolving regional climate modeling approach in decade-long simulations, J. Geophys. Res. Atmos., 119, 7889–7907, https://doi.org/10.1002/2014JD021478, 2014.

Bennetts, D. A. and Hoskins, B. J.: Conditional symmetric instability - a possible explanation for frontal rainbands, Q. J. R. Meteorol. Soc.,
700 105, 945–962, https://doi.org/10.1002/qj.49710544615, 1979.

Binder, H.: Warm conveyor belts: cloud structure and role for cyclone dynamics and extreme events, Ph.D. thesis No.24016, ETH Zürich, [available from www.research-collection.ethz.ch/handle/20.500.11850/164982], 2016.

Binder, H., Boettcher, M., Joos, H., and Wernli, H.: The role of warm conveyor belts for the intensification of extratropical cyclones in Northern Hemisphere winter, J. Atmos. Sci., 73, 3997–4020, https://doi.org/10.1175/JAS-D-15-0302.1, 2016.

705 Birkett, H. R. and Thorpe, A. J.: Superposing semi-geostrophic potential-vorticity anomalies, Q. J. R. Meteorol. Soc., 123, 2157–2163, https://doi.org/10.1002/qj.49712354318, 1997.

Bishop, C. H. and Thorpe, A. J.: Potential vorticity and the electrostatics analogy: Quasi-geostrophic theory, Q. J. R. Meteorol. Soc., 120, 713–731, https://doi.org/10.1002/qj.49712051710, 1994.

Bony, S., Stevens, B., Frierson, D. M. W., Jakob, C., Kageyama, M., Pincus, R., Shepherd, T. G., Sherwood, S. C., Siebesma,
710 A. P., Sobel, A. H., Watanabe, M., and Webb, M. J.: Clouds, circulation and climate sensitivity, Nature Geoscience, 8, 261–268, https://doi.org/10.1038/ngeo239810.1038/ngeo2398, 2015.

Boucher, O., Randall, D., Artaxo, P., Bretherton, C., Feingold, G., Forster, P., Kerminen, V.-M., Kondo, Y., Liao, H., Lohmann, U., Rasch, P., Satheesh, S. K., Sherwood, S., Stevens, B., and Zhang, X. Y.: Clouds and aerosols, pp. 571–657, Cambridge University Press, Cambridge, UK, https://doi.org/10.1017/CBO9781107415324.016, 2013.

715 Browning, K.: Conceptual models of precipitation systems, Wea. Forecasting, 1, 23–41, https://doi.org/10.1175/1520-0434(1986)001<0023:CMOPS>2.0.CO;2, 1986.

Browning, K.: Mesoscale aspects of extratropical cyclones: An observational perspective, in: The life cycles of extratropical cyclones, edited by Shapiro, M. A. and Grønås, S., pp. 265–283, Amer. Meteorol. Soc., Boston, MA, 1999.

Caldwell, P. M., Zelinka, M. D., Taylor, K. E., and Marvel, K.: Quantifying the Sources of Intermodel Spread in Equilibrium Climate
720 Sensitivity, J. Climate, 29, 513–524, https://doi.org/10.1175/JCLI-D-15-0352.1, 2016.

Cao, Z. and Cho, H.-R.: Generation of moist potential vorticity in extratropical cyclones, J. Atmos. Sci., 52, 3263–3282, https://doi.org/10.1175/1520-0469(1995)052<3263:GOMPVI>2.0.CO;2, 1995.

Chagnon, J. M. and Gray, S. L.: Horizontal potential vorticity dipoles on the convective storm scale, Q. J. R. Meteorol. Soc., 135, 1392–1408, https://doi.org/10.1002/qj.468, 2009.

725 Chagnon, J. M. and Gray, S. L.: A diabatically generated potential vorticity structure near the extratropical tropopause in three simulated extratropical cyclones, Mon. Wea. Rev., 143, 2337–2347, https://doi.org/10.1175/MWR-D-14-00092.1, 2015.

Chagnon, J. M., Gray, S. L., and Methven, J.: Diabatic processes modifying potential vorticity in a North Atlantic cyclone, Q. J. R. Meteorol. Soc., 139, 1270–1282, https://doi.org/10.1002/qj.2037, 2013.

Clark, P. A., Browning, K. A., and Wang, C.: The sting at the end of the tail: Model diagnostics of fine-scale three-dimensional structure of

730 the cloud head, Q. J. R. Meteorol. Soc., 131, 2263–2292, https://doi.org/10.1256/qj.04.36, 2005.

Clarke, S. J., Gray, S. L., and Roberts, N. M.: Downstream influence of mesoscale convective systems: Part 1, influence on forecast evolution, Q. J. R. Meteorol. Soc., https://doi.org/10.1002/qj.3593, 2019.

Crespo, J. A. and Posselt, D. J.: A-Train-based case study of stratiform - convective transition within a warm conveyor belt, Mon. Wea. Rev., 144, 2069–2084, https://doi.org/10.1175/MWR-D-15-0435.1, 2016.

735 Davies, H. and Didone, M.: Diagnosis and dynamics of forecast error growth, Mon. Wea. Rev., 141, 2483–2501, https://doi.org/10.1175/MWR-D-12-00242.1, 2013.

Davis, C. A. and Weisman, M. L.: Balanced dynamics of mesoscale vortices produced in simulated convective Systems, J. Atmos. Sci., 51, 2005–2030, https://doi.org/10.1175/1520-0469(1994)051<2005:BDOMVP>2.0.CO;2, 1994.

Doms, G. and Baldauf, M.: A description of the non-hydrostatic regional COSMO model. Part I: Dynamics and numerics, Deutscher Wet-

740 terdienst, p. 158, [available from www2.cosmo-model.org/content/model/documentation/core/cosmoDyncsNumcs.pdf], 2015.

Done, J. M., Craig, G. C., Gray, S. L., Clark, P. A., and Gray, M. E. B.: Mesoscale simulations of organized convection: Importance of convective equilibrium, Q. J. R. Meteorol. Soc., 132, 737–756, https://doi.org/10.1256/qj.04.84, 2006.

Eckhardt, S., Stohl, A., Wernli, H., James, P., Forster, C., and Spichtinger, N.: A 15-Year climatology of warm conveyor belts, J. Climate, 17, 218–237, https://doi.org/10.1175/1520-0442(2004)017<0218:AYCOWC>2.0.CO;2, 2004.

745 Flaounas, E., Lagouvardos, K., Kotroni, V., Claud, C., Delanoe, J., Flamant, C., Madonna, E., and Wernli, H.: Processes leading to heavy precipitation associated with two Mediterranean cyclones observed during the HyMeX SOP1, Q. J. R. Meteorol. Soc., 142, 275–286, https://doi.org/10.1002/qj.2618, 2016.

Flaounas, E., Kotroni, V., Lagouvardos, K., Gray, S. L., Rysman, J.-F., and Claud, C.: Heavy rainfall in Mediterranean cyclones. Part 1: contribution of deep convection and warm conveyor belt, Clim. Dyn., 50, 2935–2949, https://doi.org/10.1007/s00382-017-3783-x, 2018.

750 Grams, C. M., Wernli, H., Boettcher, M., Čampa, J., Corsmeier, U., Jones, S. C., Keller, J. H., Lenz, C.-J., and Wiegand, L.: The key role of diabatic processes in modifying the upper-tropospheric wave guide: a North Atlantic case-study, Q. J. R. Meteor. Soc., 137, 2174–2193, https://doi.org/10.1002/qj.891, 2011.

Harrold, T.: Mechanisms influencing the distribution of precipitation within baroclinic disturbances, Q. J. R. Meteorol. Soc., 99, 232–251, https://doi.org/10.1002/qj.49709942003, 1973.

755 Harvey, B. J., Methven, J., and Ambaum, M. H. P.: Rossby wave propagation on potential vorticity fronts with finite width, J. Fluid Mech., 794, 775–797, https://doi.org/10.1017/jfm.2016.180, 2016.

Hitchman, M. H. and Rowe, S. M.: On the similarity of lower-stratospheric potential vorticity dipoles above tropical and midlatitude deep convection, J. Atmos. Sci., 74, 2593–2613, https://doi.org/10.1175/JAS-D-16-0239.1, 2017.

Hoskins, B.: Potential vorticity and the PV perspective, Adv. Atmos. Sci., 32, 2–9, https://doi.org/10.1007/s00376-014-0007-8, 2015.

760 Hoskins, B. J., McIntyre, M. E., and Robertson, A. W.: On the use and significance of isentropic potential vorticity maps, Q. J. R. Meteorol. Soc., 111, 877–946, https://doi.org/10.1002/qj.49711147002, 1985.

Joos, H.: Warm conveyor belts and their role for cloud radiative forcing in the extratropical storm tracks, J. Climate, 32, 5325–5343, https://doi.org/10.1175/JCLI-D-18-0802.1, 2019.

Joos, H. and Forbes, R. M.: Impact of different IFS microphysics on a warm conveyor belt and the downstream flow evolution, Q. J. R. 765 Meteorol. Soc., 142, 2727–2739, https://doi.org/10.1002/qj.2863, 2016.

Joos, H. and Wernli, H.: Influence of microphysical processes on the potential vorticity development in a warm conveyor belt: a case-study with the limited-area model COSMO, Q. J. R. Meteorol. Soc., 138, 407–418, https://doi.org/10.1002/qj.934, 2012.

Joos, H., Spichtinger, P., Reutter, P., and Fusina, F.: Influence of heterogeneous freezing on the microphysical and radiative properties of orographic cirrus clouds, Atmos. Chem. Phys., 14, 6835–6852, https://doi.org/10.5194/acp-14-6835-2014, 2014.

770 Krämer, M., Rolf, C., Luebke, A., Afchine, A., Spelten, N., Costa, A., Meyer, J., Zöger, M., Smith, J., Herman, R. L., Buchholz, B., Ebert, V., Baumgardner, D., Borrmann, S., Klingebiel, M., and Avallone, L.: A microphysics guide to cirrus clouds – Part 1: Cirrus types, Atmos. Chem. Phys., 16, 3463–3483, https://doi.org/10.5194/acp-16-3463-2016, 2016.

Kuo, Y.-H., Shapiro, M. A., and Donall, E. G.: The interaction between baroclinic and diabatic processes in a numerical simulation of a rapidly intensifying extratropical marine cyclone, Mon. Wea. Rev., 119, 368–384, https://doi.org/10.1175/1520-775 0493(1991)119<0368:TIBBAD>2.0.CO;2, 1991.

Luebke, A. E., Afchine, A., Costa, A., Grooß, J.-U., Meyer, J., Rolf, C., Spelten, N., Avallone, L. M., Baumgardner, D., and Krämer, M.: The origin of midlatitude ice clouds and the resulting influence on their microphysical properties, Atmos. Chem. Phys., 16, 5793–5809, https://doi.org/10.5194/acp-16-5793-2016, 2016.

Madonna, E., Wernli, H., Joos, H., and Martius, O.: Warm conveyor belts in the ERA-Interim dataset (1979-2010). Part I: Climatology and 780 potential vorticity evolution, J. Climate, 27, 3–26, https://doi.org/10.1175/JCLI-D-12-00720.1, 2014.

Martínez-Alvarado, O. and Plant, R. S.: Parametrized diabatic processes in numerical simulations of an extratropical cyclone, Q. J. R. Meteorol. Soc., 140, 1742–1755, https://doi.org/10.1002/qj.2254, 2014.

Martínez-Alvarado, O., Joos, H., Chagnon, J., Boettcher, M., Gray, S. L., Plant, R. S., Methven, J., and Wernli, H.: The dichotomous structure of the warm conveyor belt, Q. J. R. Meteorol. Soc., 140, 1809–1824, https://doi.org/10.1002/qj.2276, 2014.

785 Martínez-Alvarado, O., Madonna, E., Gray, S. L., and Joos, H.: A route to systematic error in forecasts of Rossby waves, Q. J. R. Meteorol. Soc., 142, 196–210, https://doi.org/10.1002/qj.2645, 2016.

Miltenberger, A. K., Pfahl, S., and Wernli, H.: An online trajectory module (version 1.0) for the nonhydrostatic numerical weather prediction model COSMO, Geosci. Model Dev., 6, 1989–2004, https://doi.org/10.5194/gmd-6-1989-2013, 2013.

Miltenberger, A. K., Roches, A., Pfahl, S., and Wernli, H.: Online trajectory module in COSMO: A short user guide, COSMO Technical 790 Report 24, 2014.

Neiman, P. J., Shapiro, M. A., and Fedor, L. S.: The life cycle of an extratropical marine cyclone. Part II: Mesoscale structure and diagnostics, Mon. Wea. Rev., 121, 2177–2199, https://doi.org/10.1175/1520-0493(1993)121<2177:TLCOAE>2.0.CO;2, 1993.

Oertel, A., Boettcher, M., Joos, H., Sprenger, M., Konow, H., Hagen, M., and Wernli, H.: Convective activity in an extratropical cyclone and its warm conveyor belt – a case-study combining observations and a convection-permitting model simulation, Q. J. R. Meteorol. Soc., 795 145, 1406–1426, https://doi.org/10.1002/qj.3500, 2019.

Pfahl, S., Madonna, E., Boettcher, M., Joos, H., and Wernli, H.: Warm conveyor belts in the ERA-Interim data set (1979-2010). Part II: Moisture origin and relevance for precipitation, J. Climate, 27, 27–40, https://doi.org/10.1175/JCLI-D-13-00223.1, 2014.

Pomroy, H. R. and Thorpe, A. J.: The evolution and dynamical role of reduced upper-tropospheric potential vorticity in intensive observing period one of FASTEX, Mon. Wea. Rev., 128, 1817–1834, https://doi.org/10.1175/1520-0493(2000)128<1817:TEADRO>2.0.CO;2, 2000.

Rasp, S., Selz, T., and Craig, G.: Convective and slantwise trajectory ascent in convection-permitting simulations of midlatitude cyclones, Mon. Wea. Rev., 144, 3961–3976, https://doi.org/10.1175/MWR-D-16-0112.1, 2016.

Raymond, D. J. and Jiang, H.: A theory for long-lived mesoscale convective systems, J. Atmos. Sci., 47, 3067–3077, https://doi.org/10.1175/1520-0469(1990)047<3067:ATFLLM>2.0.CO;2, 1990.

Rodwell, M. J., Magnusson, L., Bauer, P., Bechtold, P., Bonavita, M., Cardinali, C., Diamantakis, M., Earnshaw, P., Garcia-Mendez, A., Isaksen, L., Källén, E., Klocke, D., Lopez, P., McNally, T., Persson, A., Prates, F., and Wedi, N.: Characteristics of occasional poor medium-range weather forecasts for Europe, Bull. Am. Meteor. Soc., 94, 1393–1405, https://doi.org/10.1175/BAMS-D-12-00099.1, 2013.

Rossa, A., Wernli, H., and Davies, H. C.: Growth and decay of an extra-tropical cyclone's PV-tower, Meteorol. Atmos. Phys., 73, 139–156, https://doi.org/10.1007/s007030050070, 2000.

Rowe, S. M. and Hitchman, M. H.: On the role of inertial instability in stratosphere–troposphere exchange near midlatitude cyclones, J. Atmos. Sci., 72, 2131–2151, https://doi.org/10.1175/JAS-D-14-0210.1, 2015.

Rowe, S. M. and Hitchman, M. H.: On the Relationship between Inertial Instability, Poleward Momentum Surges, and Jet Intensifications near Midlatitude Cyclones, J. Atmos. Sci., 73, 2299–2315, https://doi.org/10.1175/JAS-D-15-0183.1, 2016.

Schäfler, A. and Harnisch, F.: Impact of the inflow moisture on the evolution of a warm conveyor belt, Q. J. R. Meteorol. Soc., 141, 299–310, https://doi.org/10.1002/qj.2360, 2015.

Schäfler, A., Craig, C., Wernli, H., Arbogast, P., Doyle, J. D., McTaggart-Cowan, R., Methven, J., Rivière, G., Ament, F., Boettcher, M., Bramberger, M., Cazenave, Q., Cotton, R., Crewell, S., Delanoë, J., Dörnbrack, A., Ehrlich, A., Ewald, F., Fix, A., Grams, C. M., Gray, S. L., Grob, H., Groß, S., Hagen, M., Harvey, B., Hirsch, L., Jacob, M., Kölling, T., Konow, H., Lemmerz, C., Lux, O., Magnusson, L., Mayer, B., Mech, M., Moore, R., Pelon, J., Quinting, J., Rahm, S., Rapp, M., Rautenhaus, M., Reitebuch, O., Reynolds, C. A., Sodemann, H., Spengler, T., Vaughan, G., Wendisch, M., Wirth, M., Witschas, B., Wolf, K., and Zinner, T.: The North Atlantic Waveguide and Downstream Impact Experiment, Bull. Am. Meteor. Soc., 99, 1607–1637, https://doi.org/10.1175/BAMS-D-17-0003.1, 2018.

Schmetz, J., Pili, P., Tjemkes, S., Just, D., Kerkmann, J., Rota, S., and Ratier, A.: An Introduction to Meteosat Second Generation (MSG), Bull. Am. Meteor. Soc., 83, 977–992, https://doi.org/10.1175/1520-0477(2002)083<0977:AITMSG>2.3.CO;2, 2002.

Schultz, D. M. and Schumacher, P. N.: The use and misuse of conditional symmetric instability, Mon. Wea. Rev., 127, 2709–2732, https://doi.org/10.1175/1520-0493(1999)127<2709:TUAMOC>2.0.CO;2, 1999.

Schultz, D. M., Schumacher, P. N., and Doswell, C. A.: The intricacies of instabilities, Mon. Wea. Rev., 128, 4143–4148, https://doi.org/10.1175/1520-0493(2000)129<4143:TIOI>2.0.CO;2, 2000.

Selz, T. and Craig, G.: Upscale error growth in a high-resolution simulation of a summertime weather event over Europe, Mon. Wea. Rev., 143, 813–827, 2015.

Sherwood, S. C.: On moist instability, Mon. Wea. Rev., 128, 4139–4142, https://doi.org/10.1175/1520-0493(2000)129<4139:OMI>2.0.CO;2, 2000.

Shutts, G.: Idealized numerical simulations of mesoscale convective systems and their implications for forecast error, Q. J. R. Meteorol. Soc., 143, 1608–1619, https://doi.org/10.1002/qj.3031, 2017.

Siedersleben, S. K. and Gohm, A.: The missing link between terrain-induced potential vorticity banners and banded convection, Mon. Wea. Rev., 144, 4063–4080, https://doi.org/10.1175/MWR-D-16-0042.1, 2016.

Spreitzer, E., Attinger, R., Boettcher, M., Forbes, R., Wernli, H., and Joos, H.: Modification of potential vorticity near the tropopause by nonconservative processes in the ECMWF model, J. Atmos. Sci., 76, 1709–1726, https://doi.org/10.1175/JAS-D-18-0295.1, 2019.

Stoelinga, M. T.: A potential vorticity-based study of the role of diabatic heating and friction in a numerically simulated baroclinic cyclone, Mon. Wea. Rev., 124, 849–874, https://doi.org/10.1175/1520-0493(1996)124<0849:APVBSO>2.0.CO;2, 1996.

840 Thompson, C. F., Schultz, D. M., and Vaughan, G.: A global climatology of tropospheric inertial instability, J. Atmos. Sci., 75, 805–825, https://doi.org/10.1175/JAS-D-17-0062.1, 2018.

Thorpe, A. J. and Bishop, C. H.: Potential vorticity and the electrostatics analogy: Ertel—Rossby formulation, Q. J. R. Meteorol. Soc., 121, 1477–1495, https://doi.org/10.1002/qj.49712152612, 1995.

Tiedtke, M.: A comprehensive mass flux scheme for cumulus parameterization in large-scale models, Mon. Wea. Rev., 117, 1779–1800,

845 https://doi.org/10.1175/1520-0493(1989)117,1779:ACMFSF.2.0.CO;2, 1989.

Vial, J., Dufresne, J.-L., and Bony, S.: On the interpretation of inter-model spread in CMIP5 climate sensitivity estimates, Clim. Dyn., 41, 3339–3362, https://doi.org/10.1007/s00382-013-1725-9, 2013.

Volonté, A., Clark, P. A., and Gray, S. L.: The role of mesoscale instabilities in the sting-jet dynamics of windstorm Tini, Q. J. R. Meteorol. Soc., 144, 877–899, https://doi.org/10.1002/qj.3264, 2018.

850 Weijenborg, C., Friederichs, P., and Hense, A.: Organisation of potential vorticity on the mesoscale during deep moist convection, Tellus, 67, 25 705, https://doi.org/10.3402/tellusa.v67.25705, 2015.

Weijenborg, C., Chagnon, J. M., Friederichs, P., Gray, S. L., and Hense, A.: Coherent evolution of potential vorticity anomalies associated with deep moist convection, Q. J. R. Meteorol. Soc., 143, 1254–1267, https://doi.org/10.1002/qj.3000, 2017.

Wernli, H.: A Lagrangian-based analysis of extratropical cyclones. II: A detailed case-study, Q. J. R. Meteor. Soc., 123, 1677–1706, 1997.

855 Wernli, H. and Davies, H. C.: A Lagrangian-based analysis of extratropical cyclones. I: The method and some applications, Q. J. R. Meteor. Soc., 123, 467–489, https://doi.org/10.1256/smsqj.53810, 1997.

Wernli, H., Boettcher, M., Joos, H., Miltenberger, A. K., and Spichtinger, P.: A trajectory-based classification of ERA-Interim ice clouds in the region of the North Atlantic storm track, Geophys. Res. Letters, 43, 6657–6664, https://doi.org/10.1002/2016GL068922, 2016.

Zhang, Y., Macke, A., and Albers, F.: Effect of crystal size spectrum and crystal shape on stratiform cirrus radiative forcing, Atmos. Res.,

860 52, 59–75, https://doi.org/10.1016/S0169-8095(99)00026-5, 1999.
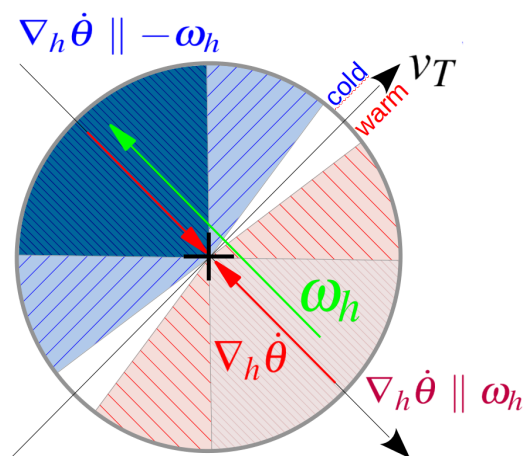
Figure 1. Conceptual model of upper-level PV modification by a convective updraft (+) that is located in an environment with background horizontal vorticity. Shown are thermal wind vector ($\mathbf{v_T}$, black) with the cold air on the left, the horizontal vorticity vector ($\boldsymbol{\omega}_h$, green), the diabatic heating gradients pointing toward the convective updraft ($\nabla_h \dot{\theta}$, red) and the regions where PV is destroyed (blue hatching) and where PV is generated (red hatching), because $\nabla_h \dot{\theta} \parallel -\boldsymbol{\omega}_h$ and $\nabla_h \dot{\theta} \parallel \boldsymbol{\omega}_h$, respectively (cf. eq. 4). The density of the hatching schematically represents the degree of PV change. See text for details.
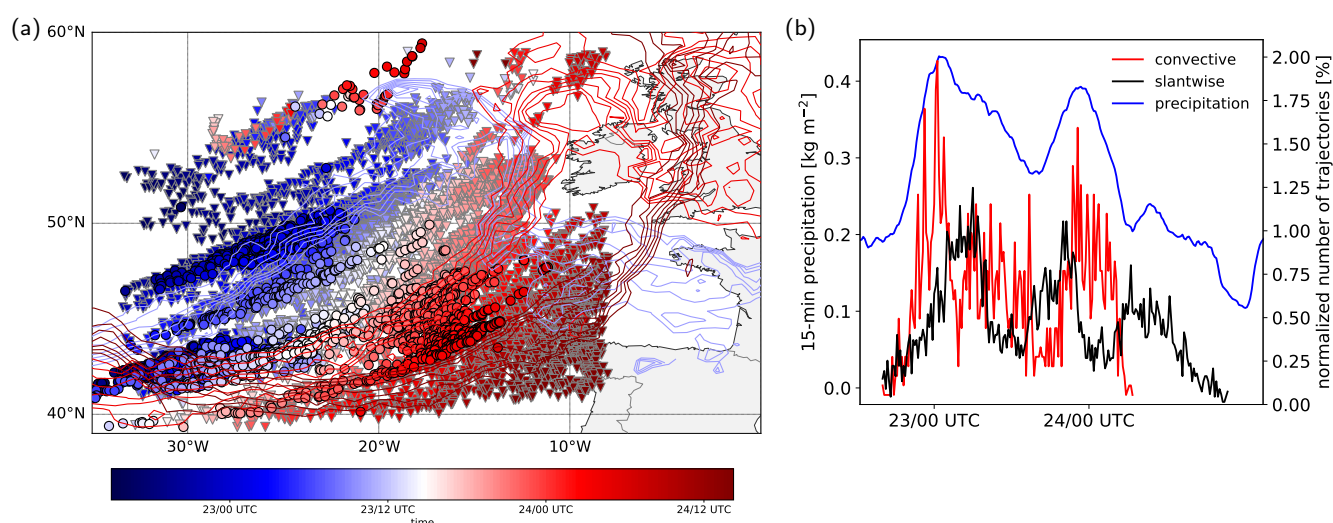
Figure 2. (a) Location of convective (black outlined circles) and slantwise (grey outlined triangle) WCB trajectories at the start of the fastest 400-hPa ascent phase. Color indicates the time evolution (blue 23 Sep, red 24 Sep). The evolution of the frontal structure is indicated by θ at 850 hPa (contours, every 0.5 K starting at 292 K) of selected times (10 UTC 23 Sep, 04 UTC 24 Sep and 22 UTC 24 Sep). **(b)** Temporal evolution of number of selected convective (red) and slantwise (black) WCB trajectories normalized by the absolute number of selected trajectories in each category and evolution of 15-minute precipitation averaged over the WCB domain shown in **(a)**. Note that for the domain-averaged precipitation only grid points with non-zero precipitation were considered.
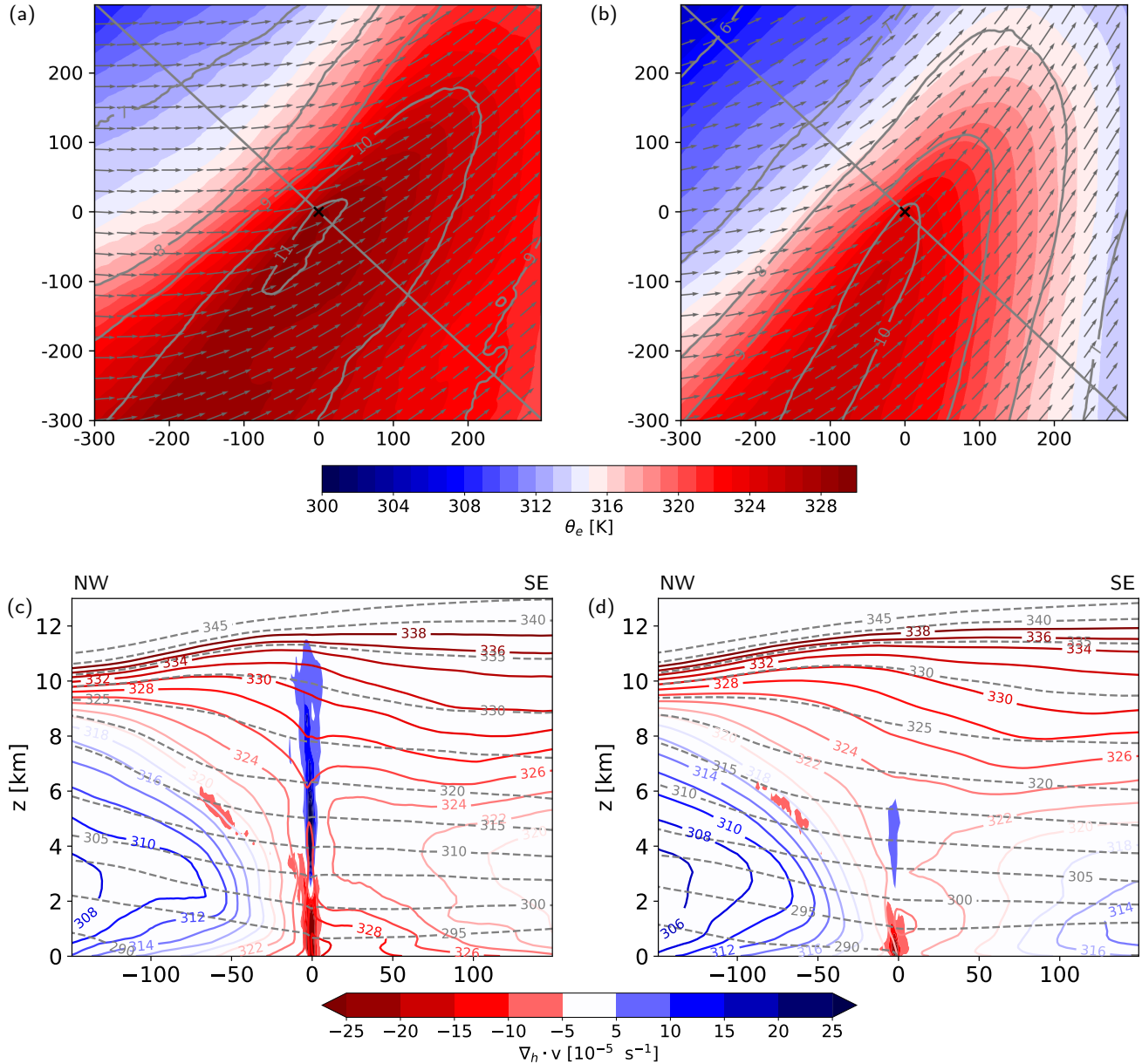
Figure 3. (a,b) Horizontal cross-section composites of θ_e at 900 hPa (colours, in K), specific humidity (grey contours, every $1\,\mathrm{g\,kg^{-1}}$) and wind at 900 hPa (arrows) for **(a)** convective WCB trajectories and **(b)** slantwise WCB trajectories at the start of the fastest 400 hPa-ascent. The axes' dimensions denote the distance from the WCB air parcel locations marked as '×' (in km). **(c,d)** Vertical cross-section composite along the northwest-southeast orientated lines shown in **(a,b)** for horizontal wind divergence (colours, in s^{-1}), equivalent potential temperature (θ_e, red - blue lines, every 2 K) and potential temperature (θ, grey dashed lines, every 5 K) for **(c)** convective and **(d)** slantwise WCB trajectories at the start of the fastest 400-hPa ascent. The x-axis denotes the distance from the WCB air parcel locations (in km).
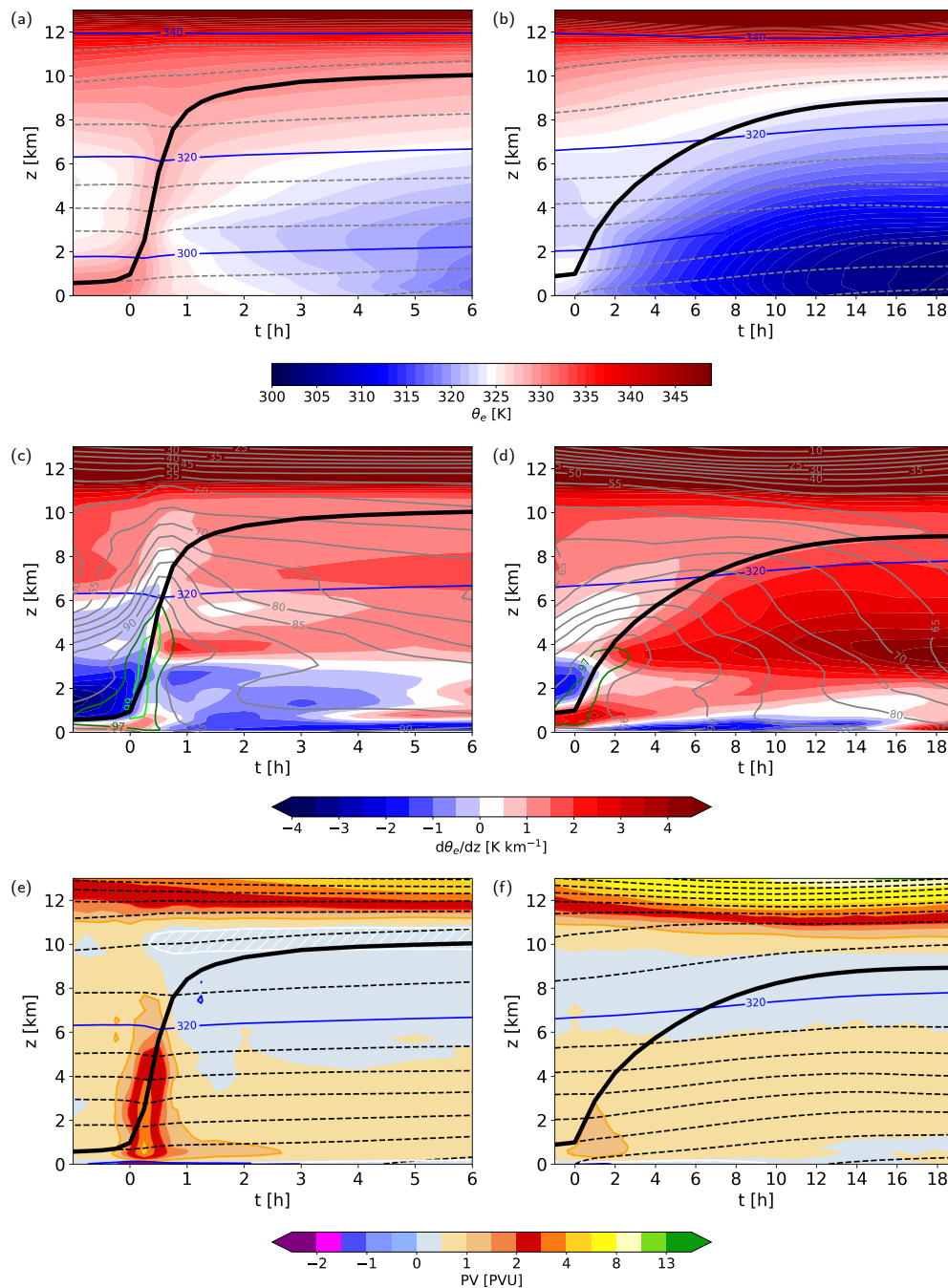
Figure 4. Vertical cross-section composites following the motion of the trajectories for **(a,c,e)** convective WCB trajectories and **(b,d,f)** slantwise WCB trajectories for **(a,b)** equivalent potential temperature (θ_e, colours, in K), potential temperature (θ, grey dashed lines, every 5 K) and the 320-K isentrope (blue line); **(c,d)** potential instability ($\mathrm{d}\theta/\mathrm{d}z$, colours, in $\mathrm{K\,km}^{-1}$), the 320-K isentrope (blue line), and relative humidity (RH, grey contours, in %; 97% and 99% RH contours are highlighted in green and lime); **(e,f)** PV (colours, in PVU), isentropes (dashed lines, every 5 K), the 320-K isentrope (blue line), and in **(e)** low static stability layers ($\mathrm{d}\theta/\mathrm{d}z \leq 2\,\mathrm{K\,km}^{-1}$, white contour and hatching). Note the different time axis in **(a,c,e)** and **(b,d,f)**.
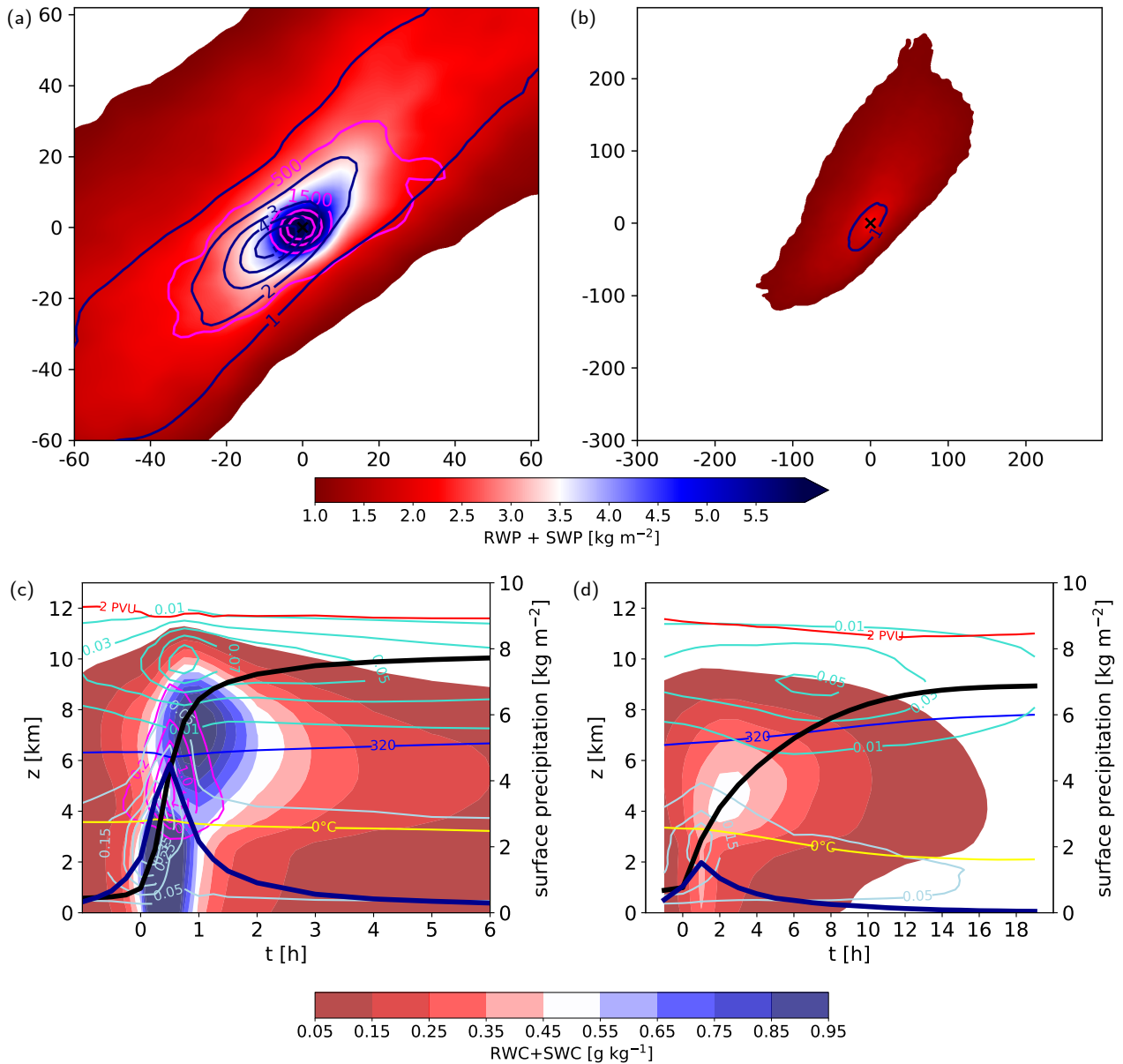
Figure 5. (a,b) As Fig. 3a,b but for vertically integrated rain and snow water content (RWP + SWP, colours, in $\mathrm{g\,m}^{-2}$), vertically integrated graupel water content (magenta contours, every $500\,\mathrm{g\,m}^{-2}$) and surface precipitation (blue contours, every $1\,\mathrm{kg\,m}^{-2}$) for **(a)** convective WCB trajectories 30 minutes after the start of the fastest 400-hPa ascent and **(b)** slantwise WCB trajectories 1 h after the start of the fastest 400-hPa ascent for; **(c,d)** as Fig. 4a,b but for hydrometeor contents (RWC + SWC, colours, in $\mathrm{g\,kg}^{-1}$; IWC, turquoise contours, every $0.02\,\mathrm{g\,kg}^{-1}$; LWC, light blue contours, every $0.1\,\mathrm{g\,kg}^{-1}$; GWC, magenta contours, every $0.4\,\mathrm{g\,kg}^{-1}$), surface precipitation (thick blue line, in $\mathrm{kg\,m}^{-2}$), $0°\mathrm{C}$-isotherm (yellow line), 320-K isentrope (blue line) and the 2-PVU tropopause (red line). Note the different spatial dimensions of **(a)** and **(b)** and the different time axis in **(c)** and **(d)**.
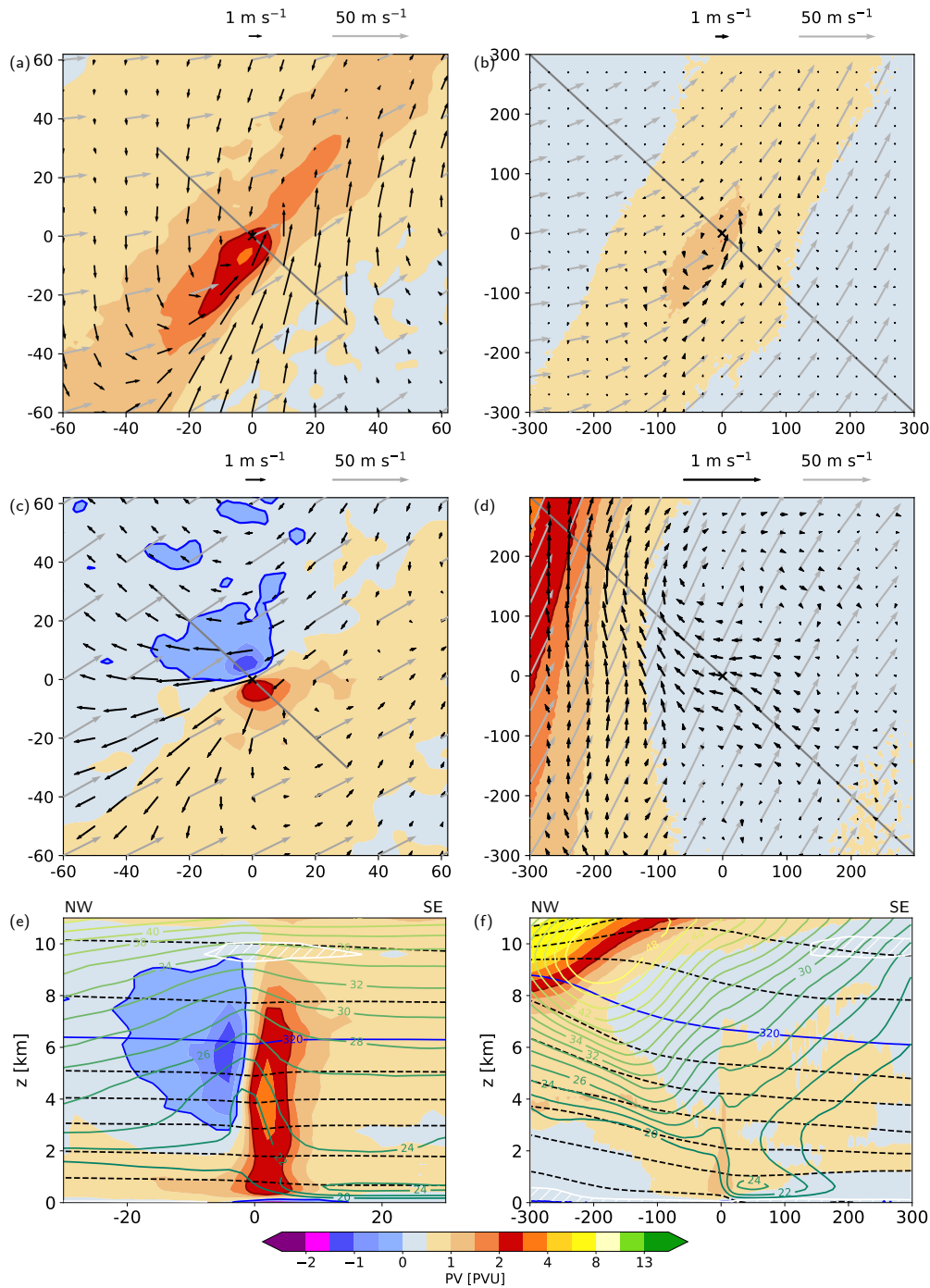
Figure 6. (a-d) As Fig. 3a,b but for PV (colours, in PVU), wind speed (grey arrows, in $\mathrm{m\,s^{-1}}$) and 2-h circulation anomalies (black arrows, in $\mathrm{m\,s^{-1}}$) at **(a,b)** 800 m and **(c,d)** 320 K for **(a,c)** convective WCB trajectories 30 minutes after the start of the fastest 400-hPa ascent, and for **(b,d)** slantwise WCB trajectories **(b)** 1 h and **(d)** 10 h after the start of the fastest 400-hPa ascent. **(e,f)** Vertical cross-section composite along the northwest-southeast orientated lines shown in **(a,b)** of PV (colours, in PVU), wind speed (green contours, every $2\,\mathrm{m\,s^{-1}}$), isentropes (dashed lines, every 5 K), the 320-K isentrope (blue line) and low static stability layers ($\mathrm{d}\theta/\mathrm{d}z \leq 2\,\mathrm{K\,km^{-1}}$, white contour and hatching) for **(e)** convective WCB trajectories 30 minutes and **(f)** slantwise WCB trajectories 1 h after the start of the fastest 400-hPa ascent. Note the different spatial dimensions for the convective and slantwise WCB trajectories.
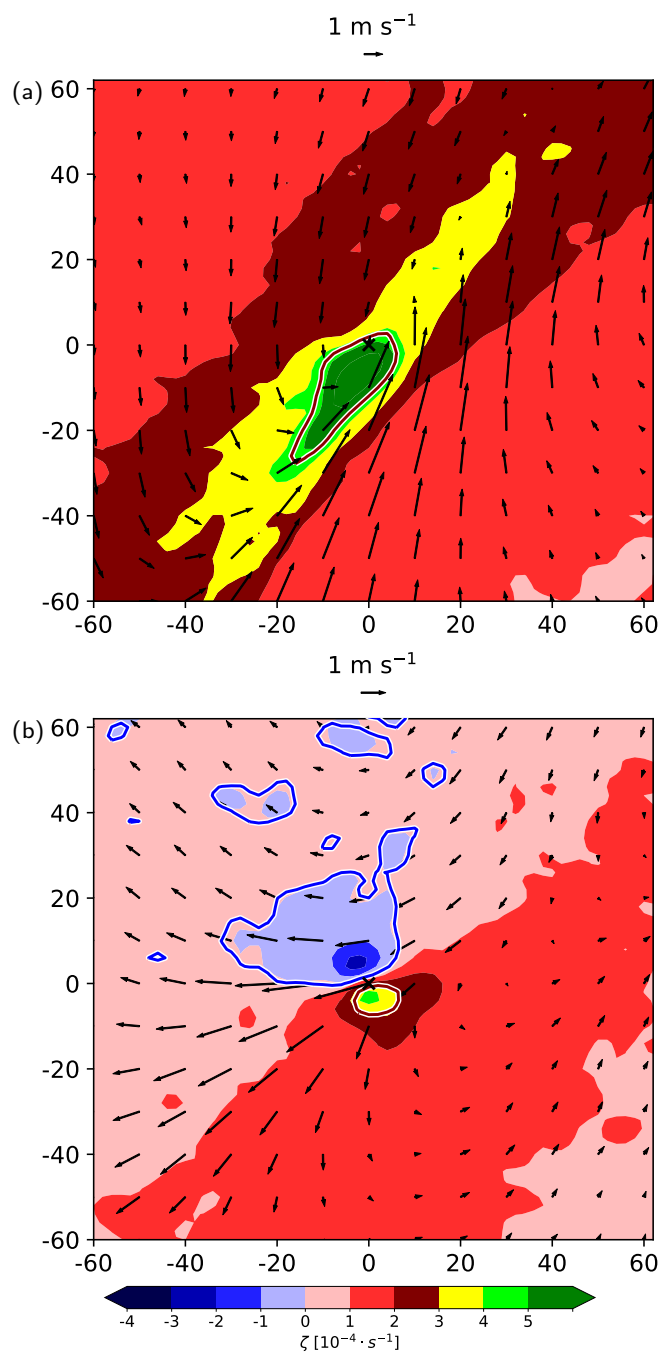
Figure 7. As Fig. 6a,c but for absolute vertical vorticity ($f + \zeta$, colours, in s^{-1}) and 2-h circulation anomalies (black arrows, in $\mathrm{m\,s}^{-1}$) at **(a)** 800 m and **(b)** 320 K for convective WCB trajectories 30 minutes after the start of the fastest 400-hPa ascent. The 0 and 2 PVU contour lines are shown in blue and red, respectively.
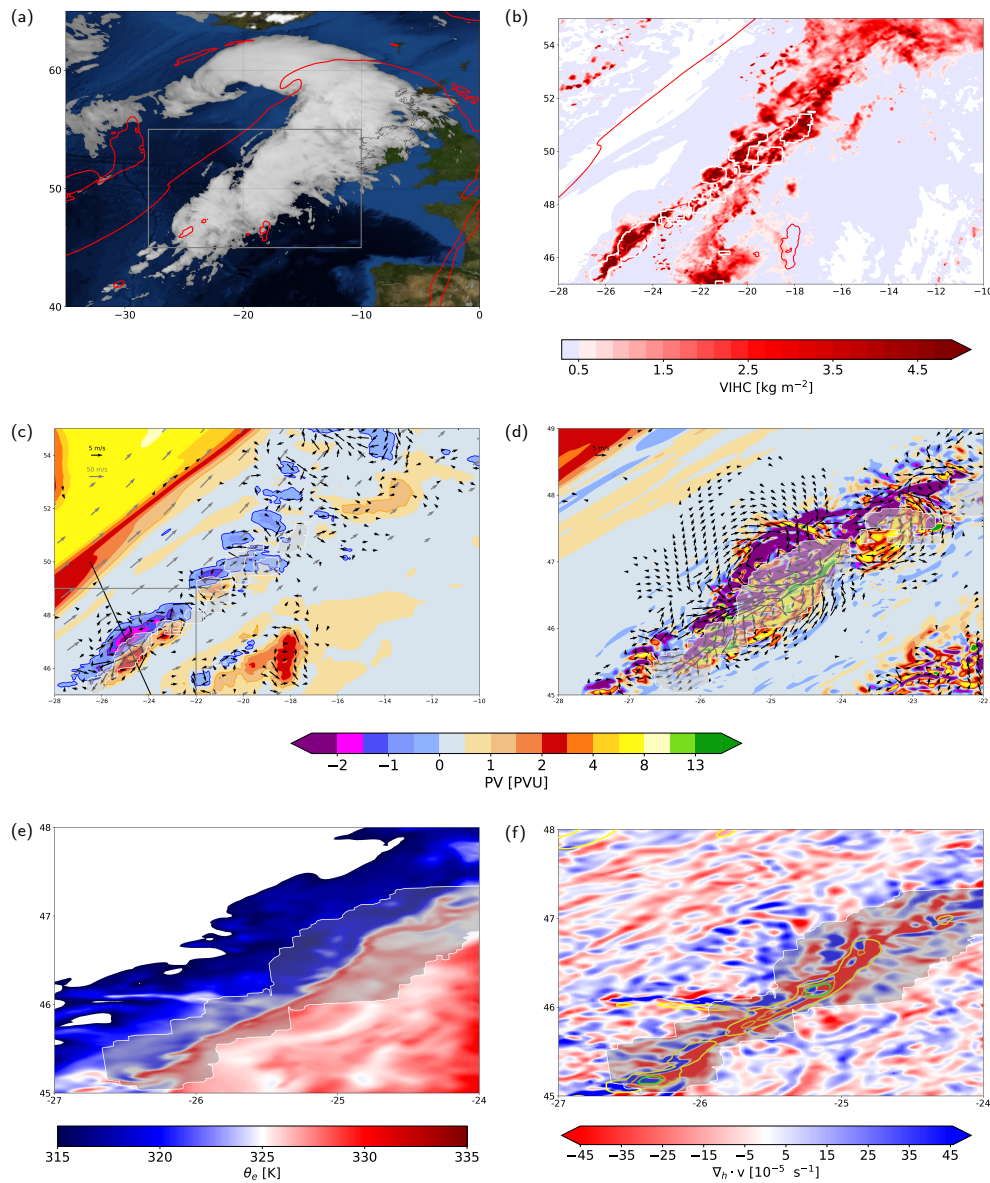
Figure 8. Example of embedded convection in the WCB at 09 UTC 23 Sep 2016. **(a)** IR satellite image of the large-scale cloud structure [10.8 μm, EUMETSAT, Schmetz et al. (2002)] and 2 PVU contour at 320 K (red line); **(b)** vertically integrated hydrometeor content (VIHC, colours for VIHC $> 5\,\mathrm{g\,m^{-2}}$, in $\mathrm{kg\,m^{-2}}$) for the region outlined in **(a)** (grey box), envelope of rapid WCB ascent (white outline) and 2 PVU contour at 320 K (red line); **(c)** coarse-grained PV at 320 K (colours, in PVU; purple, blue, orange and red contour lines show -1, 0, 1 and 2 PVU; see text for details), 2-h circulation anomalies at 320 K (black arrows), wind speed at 320 K (grey arrows) and envelope of rapid WCB ascent (white outline); **(d)** enlargment of embedded convection shown in **(c)** (grey box) with PV at 320 K from the original 2-km model grid, 2-h circulation anomalies at 320 K (black arrows) and envelope of rapid WCB ascent (white outline); **(e)** enlargement of embedded convection shown in **(c)** with equivalent potential temperature at 900 hPa (θ_e, colours, in K) and envelope for rapid WCB ascent (white outline); **(f)** as **(e)** but for low-level wind divergence at 295 K (colours, in $\mathrm{s^{-1}}$), PV at 295 K (yellow, lime and magenta contour lines at 2, 4, and 5 PVU) and envelope of rapid WCB ascent (white outline).
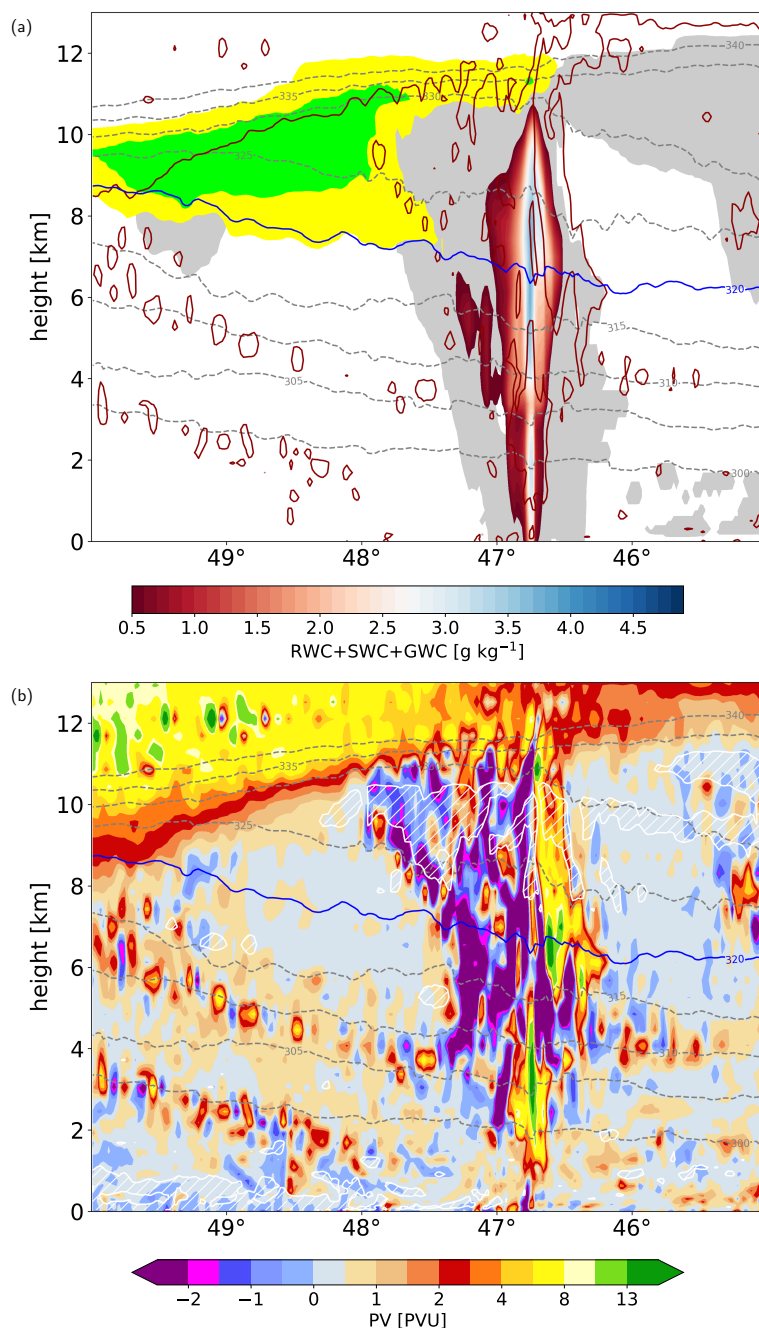
Figure 9. Vertical cross-section through the PV dipole shown in Fig. 8c (black line) at 09 UTC 23 Sep 2016 for **(a)** sum of rain, snow and graupel water content (RWC + SWC + GWC, colours, in $\mathrm{g\,kg^{-1}}$), cloudy region (grey shading, hydrometeor content $> 1\,\mathrm{mg\,kg^{-1}}$), upper-level jet (yellow and green shading at 55 and $60\,\mathrm{m\,s^{-1}}$) and 2 PVU contour (dark red line), and **(b)** PV (colours, in PVU) and low static stability layer ($\mathrm{d}\theta/\mathrm{d}z \leq 2\,\mathrm{K\,km^{-1}}$, white contour and hatching). Isentropes (dashed contours, every 5 K) and the 320-K isentrope (blue line) are shown in both panels.
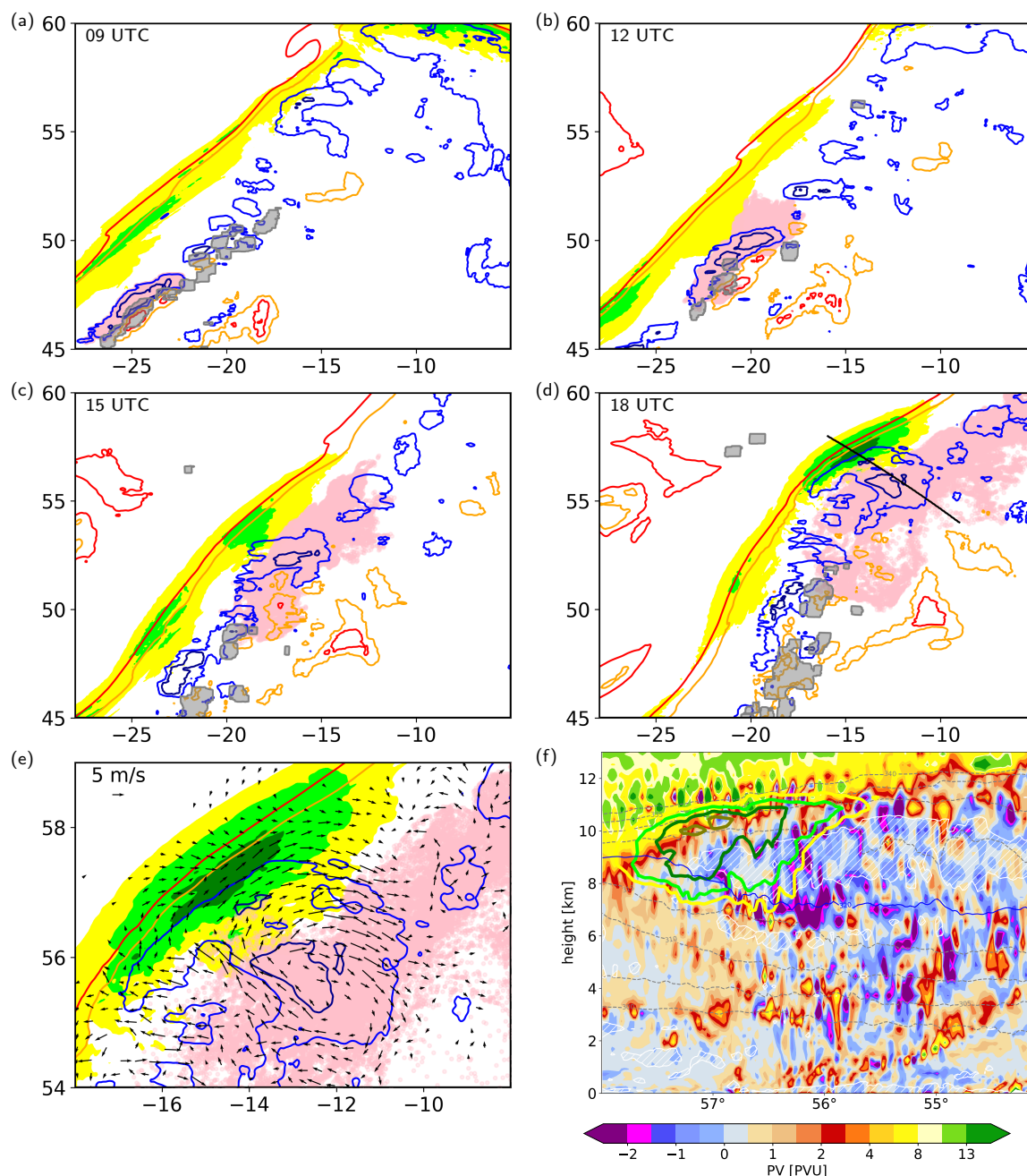
Figure 10. Spatially averaged upper-level PV at 320 K (dark blue, blue, orange and red contours at -1, 0, 1 and 2 PVU), upper-level jet at 320 K (yellow and green colours at 55, 60 and 65 m s^{-1}) and envelope of rapid WCB ascent (grey contour and shading) at **(a)** 09 UTC, **(b)** 12 UTC, **(c)** 15 UTC and **(d)** 18 UTC 23 Sep 2016. The pink shading shows the positions of forward trajectories initialized in a region of convectively produced negative PV between 315 and 325 K at 09 UTC; **(e)** is an enlargment of **(d)** and additionally shows the 2-h circulation anomaly (black arrows); **(f)** Vertical cross-section along the line shown in **(d)** for PV (colours, in PVU), potential temperature (grey dashed, every 5 K), 320-K isentrope (blue line), and jet (yellow and green contours, at 55, 60, 65 and 70 m s^{-1}). Low static stability (dθ/dz $\leq$ 2 K km^{-1}) is indicated by the white contour and hatching **37**
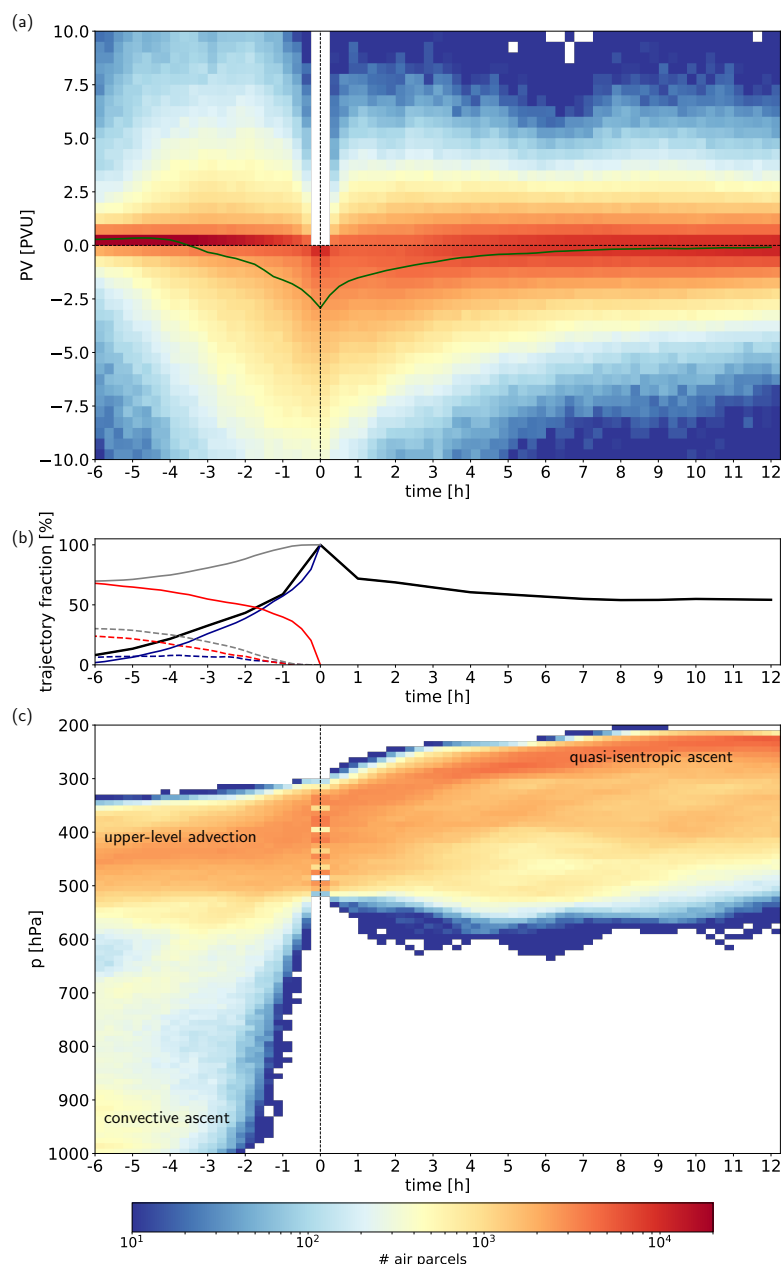
Figure 11. (a) 2D histogram of temporal evolution of PV (in PVU) for forward and backward trajectories initialized in a region of convectively produced negative PV between 315 and 325 K at 09 UTC as shown in Fig. 10a (pink shading). The time is given relative to trajectory start at 09 UTC. The green line shows PV averaged over all trajectories (in PVU). **(b)** Fraction of trajectories with a negative PV value (black, in %), the fraction of trajectories located above 600 hPa (solid grey, in %) and below 600 hPa (dashed grey, in %). Additionally, the fraction of trajectories with negative PV above 600 hPa (blue solid, in %) and below 600 hPa (blue dashed, in %), as well as the fraction of trajectories with positive PV above 600 hPa (red solid, in %) and below 600 hPa (red dashed, in %) are shown. Note that after $t=0$ h the majority of trajectories is located above 600 hPa. **(c)** As **(a)** but for pressure (in hPa).